The University Of Sheffield.

This is a repository copy of *UAV-SfM based field quantification of barchan dune celerity and morphodynamics in Gonghe Basin*.

White Rose Research Online URL for this paper:
https://eprints.whiterose.ac.uk/211532/

Version: Accepted Version

Article:

Shao, M., Lou, W., Che, X. et al. (2 more authors) (2024) UAV-SfM based field quantification of barchan dune celerity and morphodynamics in Gonghe Basin. Earth Surface Processes and Landforms, 49 (8). pp. 2380-2404. ISSN 0197-9337

https://doi.org/10.1002/esp.5834

© 2024 The Authors. Except as otherwise noted, this author-accepted version of a journal article published in Earth Surface Processes and Landforms is made available via the University of Sheffield Research Publications and Copyright Policy under the terms of the Creative Commons Attribution 4.0 International License (CC-BY 4.0), which permits unrestricted use, distribution and reproduction in any medium, provided the original work is properly cited. To view a copy of this licence, visit http://creativecommons.org/licenses/by/4.0/

Reuse

This article is distributed under the terms of the Creative Commons Attribution (CC BY) licence. This licence allows you to distribute, remix, tweak, and build upon the work, even commercially, as long as you credit the authors for the original work. More information and the full terms of the licence here: https://creativecommons.org/licenses/

Takedown

If you consider content in White Rose Research Online to be in breach of UK law, please notify us by emailing eprints@whiterose.ac.uk including the URL of the record and the reason for the withdrawal request.

White Rose university consortium
Universities of Leeds, Sheffield & York

eprints@whiterose.ac.uk
https://eprints.whiterose.ac.uk/

UAV-SfM Based Field Quantification of Barchan Dune Celerity and Morphodynamics in Gonghe Basin

Abstract

Barchan dunes do not often co-exist with grasslands. However, in Gonghe Basin, north-eastern part in Qinghai-Tibetan Plateau (QTP), China, many barchan dunes distributed on the grassland at high-altitude. Identifying celerity and morphodynamics of barchan dunes, exploring the interaction between barchans and grassland landscape can help us to better understand aeolian system sand mitigate damages. In this work, we tracked dune celerity and observed three-dimensional changes of symmetrical and asymmetrical barchan dunes in Ertala based on high resolution UAV-SfM reconstruction in short-term monitoring and discussed the factors influencing dune celerity and deformation at high-altitude. The results revealed that the barchan dunes are highly mobile with average celerity of 0.85 m/M for the whole study area. Based on observations of dune morphology and dynamics, we found: (1) The dune deformation degree in a short time is not large, but is widespread, especially in the elongated arm of asymmetric dune. The deformation of symmetric dune is symmetrical, while that of dune with extended horn is asymmetrical; (2) The sand supply, vegetation, and airflow at low air density all influence the celerity and deformation degree in the development of barchan dunes; (3) The asymmetric air flow and sediment supply are important cause of dune asymmetry. The above results help us to understand the deformation of barchan dune from the three-dimensional, especially the difference reflected by the symmetry of barchan dune at high-altitude.

Keywords: dune celerity, deformation, asymmetrical and asymmetrical barchan dunes

1 Introduction

Barchan dunes are crescentic dunes classically formed in a supply-limited environment, uni-directional wind and no vegetation (Bagnold, 1941; Cooke et al., 1993; Elbelrhiti, 2012). They are usually discrete although sometimes merged with another dune (Assis et al., 2022), and they occur in both coastal and continental regions (Finkel, 1959; Hesp and Hastings, 1998). They also form in water bodies (Hersen, 2005; Alvarez and Franklin, 2020). Barchans are migrating bedforms (Wu, 2003; Vermeesch and Drake, 2008) and their movement within a largely unimodal wind regime is relatively simple: the stoss slope of the barchan dune is eroded; and the sand is transported in creep, saltation and occasionally suspension, is deposited downwind of the brink, and is redistributed on the slip-face by avalanches (Andreotti et al., 2002; Zhang et al., 2022). One of the important actions in aeolian geomorphology has been to study and understand barchan dune celerity and deformation to better understand the risks of sand encroachment to infrastructure and down-wind at-risk communities (Long and Sharp, 1964; Zhu et al., 1964; Slattery, 1990; Bruno et al., 2018).

1.1 Spatial analysis of barchan dunes

For decades, scientists have reported results of observation and experiments on barchan dunes, and measuring their formation, erosion and deposition, activity or stability, turbulent flow structures and the size distribution of associated sand grains (Beadnell, 1910; Cornish, 1914; Finkel, 1959; Fedolovich, 1962; Jimenez et al., 1999; Andreotti et al., 2002; Baddock et al., 2011; Hamdan et al., 2016; Havivi et al., 2018; Ding et al., 2020; Zhang et al., 2022). Their celerity and morphodynamics have commonly been studied at the dune scale over several years using a combination of field and remote sensing data (Zheng et al., 2022).

Dune celerity refers to the speed of dune migration which is measured in meters per unit time (Sam et al., 2015). Measuring dune celerity can provide an unambiguous indicator of active sand transport and that is a crucial step towards understanding aeolian system operation (Muhs and Holliday, 1995; Vermeesch and Drake, 2008; Hugenholtz et al.,2012; Bryant and Baddock, 2022; Zhang et al., 2022). Traditional field surveying methods (e.g., Dong et al., 2000) offer high levels of accuracy but are time consuming and offer a limited space/time sample. There are two broad categories from a remote sensing perspective, manual tracking, and automated extraction of dune celerity (Bryant and Baddock, 2022; Zheng et al., 2022). Manual extraction of dune celerity information includes approaches such as: (i) measuring the distance between two lines in the continuous position of the dune (Gay, 1999), (ii) recording the average length of several lines drawn are common manual methods to track the dune celerity (e.g. Hunter et al., 1983), and (iii) using an area integrated method (e.g. Levin and Ben-Dor, 2004). With the development of remote sensing technology, it is possible to automated interpret dune activity by using changes in dune DEMs and spectral reflectance (e.g. Hamdan et al., 2016; Zhang et al., 2018). In recent years, COSI-Corr has been particularly notable in automated mapping dune movement and sand flux (Leprince et al., 2007; Vermeesch and Drake, 2008; Scheidt and Lancaster, 2013; Baird et al., 2019).

As an important step in dynamic monitoring of dunes, the morphodynamics of dunes has attracted significant attention (Frank and Kocurek, 1966; Sweet and Kocurek, 1990) since Zhu et al (1964) described the formation change during the evolution of dunes. In recent years, research on establishing the relationship between morphological characteristics, wind flow and the evolution of barchans have been making great progress (Finkel, 1959; Long and Sharp, 1964; Hastenrath, 1967, 1987; Tsoar, 1985; Hesp and Hastings, 1998; Bourke and Goudie, 2009). Initially, three-dimensional assessments of dune morphodynamical change (including assessment of locations of erosion and deposition) was determined via use of digital terrain data generate by use of hard and soft copy analysis of aerial photographs (e.g. Brown and Arbogast, 1999; Ojeda et al., 2005). Subsequently, LiDAR data have used to determine volume change of sand dune area (Pedersen et al., 2015). Vermeesch and Drake (2008) used COSI - Corr to calculate the dune mass flux. In some cases, it may be more effective to use field-based measurements (GPS and total station) to measure dune surface changes (Coursin, 1964; El-Sherbiny and Bofah, 1982; Dong and Huang, 2014; Guo et al., 2016).

Recent studies in numerical simulation and flume (wind tunnel) experiments have shown that the importance of dune morphological evolution has become an import research priority (Walmsley and Howard, 1985; Wippermann and Gross, 1986; Duran et al., 2010; Lv et al., 2018; Hugenholtz, 2010; Andreotti et al., 2002). At present, we still have a limited understanding of the process of changes in dune morphology, as morphodynamics analysis has traditionally been based on the assumptions associated with two-dimensional dune morphology, essentially ignoring components of the three-dimensional morphology that may be pertinent (Scheltinga, 2022). Consequently, high-frequency three-dimension DEM data are needed to resolve the observed rapid morphodynamical response of dunes to prevailing wind flow. Emerging technologies, such as the use of UAV (Unpiloted Aerial Vehicle), provide possibilities for dune morphodynamical surveying (Luo et al., 2020; Bryant and Baddock, 2022).

Dune shape and asymmetry can vary in space/time because dune morphodynamics is dynamic rarely observed in equilibrium. Also, in vegetated areas, the supply of sediment (which can be controlled by vegetation changes) can directly impact the rate of movement (Xu et al., 2015). The simplest expression of asymmetry, the horn extension, can be used to distinguish between bimodal wind conditions and dune collisions, which are factors that alter dune morphology on larger scale (Bourke, 2010; Tsoar and Parteli, 2016). It can also be used to infer upwind currents, modification of the sedimentary dynamics of barchan dunes, and, for where no data are available, local topography of an area (Bourke, 2010; Merwe et al., 2022). However, we note that these inferences cannot be drawn from a single observation of a barchan dune, and in order to be truly valid, multiple observations over different time periods are needed to fully understand the dynamics within the dune region (Merwe et al., 2022). Small-scale aeolian landforms, such as sand ripples, evolve very quickly with time. Wind tunnel experiment results show that the original particles can drift about 1 cm downward every 5 minutes (Fryberger et al., 1992). The timescale of normal ripples is minutes (Anderson, 1990), while the Mega-ripples is days (Sakamoto-Arnold, 1988) and years (Bagnold, 1941). Bogle et al (2015) repeatedly tracked the locations of several active barchan dunes at irregular intervals ranging from 24 to 169 days. Ewing et al (2015) believed that dune field was composed of different types of bedforms, which reflected the changes of environmental boundary conditions on a wide range of time scales, and dune field models of different scales and types should be analyzed at different stages. Kocurek et al (1992) made seasonal observations on some dune fields on Padre Island, Texas, and found that the dune fields would become flat in winter, and then would reconstruct in spring and summer.

In fact, most barchan dunes in nature are asymmetrical. The potential causes of the asymmetry of barchan dunes include asymmetric bidirectional wind conditions, topography, asymmetry of inflow and dune collision (Parteli et al., 2014; Tsoar and Parteli, 2016). It has been found that where the divergence angle between the main winds and secondary winds is low, the two horns remain similar and both are thick and short (Lv et al., 2016). However, when the divergence angle is obtuse, these asymmetric bimodal wind conditions will lead to the extension of the dune horn (Tsoar and Parteli, 2016; Bourke, 2010), and where the transport ratio of the two exceeds 25%, an asymmetric barchan dune may evolve into seif dune (Parteli et al., 2014). There are two classical models for the evolution of barchan dunes into seif dunes, (Bagnold, 1941; Tsoar,1984). Using numerical simulation, many scholars have conducted validation experiments, and the evolutionary mechanisms attributed to the two are a matter of debate. Some scholars suggest that there may be a threshold between the two evolutionary mechanisms (e.g. Lv et al., 2016; Robson and Bass, 2023), but others have divergent views (e.g. Tsoar and Parteli, 2016). In addition, although topography, inflow asymmetry and dune collision can cause dune asymmetry, models suggest that these factors may not cause barchan dunes to evolve into seif dune (Tsoar and Parteli, 2016). Although many studies have been carried out to investigate and model the asymmetric evolution of barchan dunes, there are some inevitable limitations. These include a lack of field observation data and the need to simplify aspects of the wind conditions. Ultimately observations of the morphological evolution of sand dunes in the field be critical in minimising model uncertainty and validate the simulation results in the laboratory.

1.2 Land degradation, dune stabilisation and mitigation in China

In recent decades, some parts of China have experienced serious land degradation, especially in the northern drylands. Desertification is the most prominent and concentrated ecological problem among them (Jiang et al., 2020). China is one of the countries seriously affected by desertification, accounting for 17.93% of its land area (Xu and Zhang, 2021). The research results show that the risk of desertification in China will increase over time by the end of this century (Huang et al., 2020), local land degradation was expanding in northern China, mainly in semi-arid areas (Guo et al., 2022). The activation and stabilization process of sand dunes is closely related to climate change, environmental changes and human activities, and has been widely concerned by the academic community. Baas and Delobel's (2022) research shows that the projected increased potential for many dune fields in China by 2100 is associated with climate changes in The Hadley circulation, tropical cyclone activity, and monsoon systems. However, human activities can also seriously interfere with them, and the changes of dune field in the symbiotic system of dune and vegetation are rarely discussed in these studies. Many works on dunes morphodynamics, stabilisation and migration have been carried out on various deserts, sandy lands and basins in China (He et al., 2011; Chen et al., 2018; Luo et al., 2019; Yang et al., 2019; Ding et al., 2020). These works contribute to our understanding of the development and evolution of aeolian dunes in different area.,

Vegetation plays an important role in dune stabilization. Sand dunes in some areas are very sensitive to the change of desert-grassland boundary. Rapid accumulation of aeolian particles will significantly change the surface, especially affecting the change of vegetation on the dunes, which in turn can also affect the spatial-temporal pattern of aeolian sand position. Studies have shown that stable sand dunes may be more and more susceptible to blowing with the gradual decline of shrub vegetation coverage (Fearnehough et al., 1998). However, in the same region, bare sand dunes and vegetated sand dunes may exist simultaneously, which is called the bistable state of dunes (Chen et al., 2021). Dune activity is regarded as an important source of information for reconstructing paleoclimate on a regional scale and predicting future climate change in arid areas (Guo et al., 2019). There are many deserts and sandy lands in China, and various types of sand dunes have developed, the movement and change of dunes have received extensive attention (Ding et al., 2020; Yang et al., 2019; Yang et al., 2021).

1.3 Aims and objectives.

As we note, there are still some challenges associated with observation of the rapid morphodynamics of dunes (Bryant and Baddock 2022; Zheng et al., 2022). In addition, our understanding of themorphodynamics of barchan dunes that coexist with vegetation in high-altitude settings (with low air density and low temperature, is poorly constrained (e.g. Dörwald et al., 2023). At the same time, field observations of the dynamic development of asymmetric barchan dunes that can augment modelling approaches (e.g. Robson and Baas., 2023) are also limited (e.g. Lü et al., 2022). The Gonghe Basin is located on the north-eastern margin of the Qinghai-Tibet Plateau (QTP, Figure 1), the north-western edge of the Asian monsoon region, at an altitude of 3400 m (Liu et al., 2014). Grassland is the main land cover type in Gonghe Basin, accounting for 79.52% of the total area, and land use for grazing (Sha et al., 2005). There are many isolated and fully active barchan dunes in the grassland in Gonghe Basin, there is a lot of vegetation growing in the interdunes, and no vegetation growing on the surface of the dunes. The results of wind tunnel experiments also show that at a certain wind speed, the sand transport capacity decreases at low air density, but the salting height increases (Han et al., 2014). Because of the difficulties in controlling air pressure and temperature, laboratory experiments cannot easily provide this understanding. Most previous studies on the effects of low density and low temperature have focused on extraterrestrial environments, such as Mars (Ryan and Henry, 1979; Iversen et al., 1976). Gonghe Basin is located at a high altitude, and the air density limits the wind erosion and transport process of sand, thus strongly affecting the airflow characteristics (Dong et al., 2017). Therefore, the barchan dunes in Gonghe Basin provide a natural experimental site for us to further understand the morphologic dynamics of dunes coexisting with the grassland landscape and reveal the migration characteristics of dunes at low density and low temperature.

We track the barchan dune celerity and assess rapid morphodynamics (t = 17 months) using DOM (Digital Orthophoto Maps) and DSM (Digital Surface Model) generated using UAV-SfM. Our observations based on dunes in the Ertala in Gonghe Basin and monitor these for the period March 2019 to August 2020. Our objectives of this study are to: (1) quantify the celerity and deformation of isolated symmetrical and asymmetrical barchan dunes coexist with vegetation at high-altitude; (2) discuss the influence of sand supply, vegetation, sand flow and high-altitude on dune celerity and deformation. (3) explore the controlling factors of asymmetric barchan dune evolution. In this paper, section 2 describes the methodology, section 3 presents the results, section 4 presents the discussion and section 5 illustrates the conclusions.

2 Study area and methodology

2.1 Study area

The Gonghe Basin is about 210 km long, 90 km wide and 30 km narrow, with a total area of 1.38×10^4 km^2, between 35°27′~36°56′N，98°46′~101°22′E, surrounded by the Qilian Mountains and the Erla Mountains of the Kunlun-Qilian Mountains. It extends from northwest to southeast in the west, and is narrow in the west and wide in the east in the shape of a gourd. It is a region where the distribution of aeolian landforms is concentrated (862 km^2) (Xu et al., 1982; Dong et al., 1993), which are distributed in upland plains and on terraces of the Yellow River. The surface of the basin is dominated by stabilized and semi-stabilized sand dunes, which are concentrated in Talatan, Mugetan and the tail reaches of Shazhuyu River (Liu et al., 2014). From west to east, three large sand belts comprising hundreds of kilometres of dune fields are proximal to the Longyangxia reservoir, which acts as a sediment sink (Shao et al., 2021). In order to investigate dune dynamics in this important and dynamic location, we selected 16 representative barchan dunes in the region of Ertala to monitor their celerity and deformation changes. The study area is located at 36.144166667°~36.150555556°N, 100.341111111°E ~100.357222222°E and covers an area of 0.9 km^2 (Figure 1).

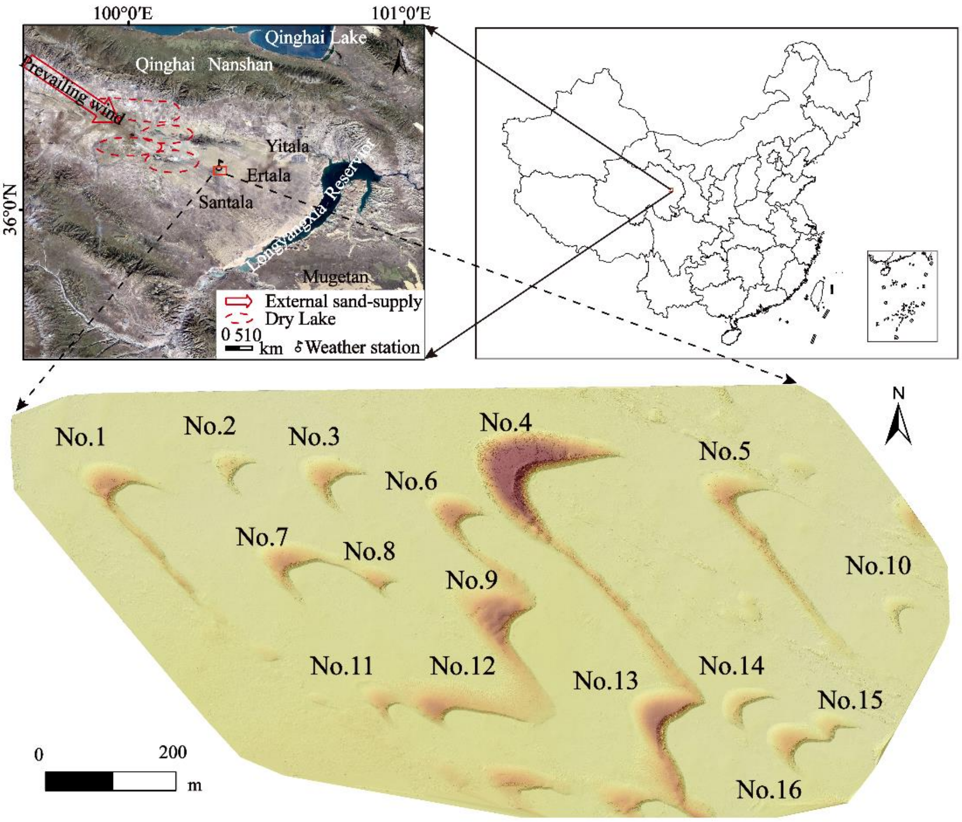

Figure 1. The location of the study area and geographical sketch map with dune number of each barchan studied.

2.2 Methodology

We went to the Ertala in March 2019, July 2019, January 2020 and August 2020 to monitored the barchan dunes by using UAVs and RTK-GPS, obtained four DOMs and DSMs of the barchan dunes in the study area through post-processing, extracted the morphological parameters and analyzed their celerity. We measured the surface airflow and sand transport characteristics of No.2 dune in the study area in April 2019 in order to further explore the morphodynamic process. This section describes our field measurement and analysis methods in detail.

2.2.1 Monitoring and measurement of 3D dune morphology

(1) Equipment

The field measurement of dune movement and morphology undertaken here was divided into two complimentary approaches: (a) UAV-SfM and (b) RTK-GPS (Real-time kinematic Global Positioning System). UAV-SfM technology is a method developed in recent years, which has the advantages of high efficiency, high precision, time, and labour saving (Balek, 2017; Qian et al., 2019; James et al., 2019; Bryant and Baddock., 2022). UAV-SfM can track topography at the centimetre level, which can overlap with requirements of topographic survey, but at a large scale (Aguera-Vega et al., 2018; Luo et al., 2020; Shao, 2021).

Here we monitored dune form variation using a DJI phantom 4 Pro V2.0 in Ertala sandy land of Gonghe Basin, Qinghai Province in March, July of 2019 and January and August of 2020, respectively. The camera image sensor of this drone is 1 inch CMOS with 20 million effective pixels, and the photo size is 5472×3078. The RTK-GPS (TOPCON, GR-3) not only has higher accuracy than the traditional total station and dumpy level measurement instruments, but also does not require visual communication, which greatly simplifies field work and has a more stable performance (Luo et al., 2019; Yang, 2019). The Figure S1 shows the UAV and RTK-GPS we used.

(2) Survey Design

The flight parameters are as follows: the flight altitude was 74 m (110 m in March 2019), the photo overlap ratio was 85%/70% (heading/sideways), the camera tilt angle was -90° (Luo et al., 2020, Shao, 2021). Sample dates, specific flight parameters, and parameters setting used in each case are shown in a supplementary file (Table 1 and Table S1).

Table 1. The flight parameters of the four monitoring using UAV

Date	Flight altitude(m)	Heading overlap (%)	Sideways overlap (%)	Camera tilt (°)	GSD(m)	Number of GCP	Number of CP
2019.03	110	85	70	-90	2.03	24	9
2019.07	74	85	70	-90	2.14	20	6
2020.01	74	85	70	-90	2.05	15	5
2020.08	74	85	70	-90	2.18	25	4

Note: GSD represents ground sampling distance, GCP represents Ground Control point, CP represent Check Point.

(3) Survey Execution

In order to improve the measurement accuracy of UAV-SfM, we established many ground control points and check points in the field. On the one hand, the matching points in the post-processing process can be increased, and on the other hand, the error can be controlled within the centimetre level. 43 ground control/check points were set, which were coordinated using RTK-GPS (TOPCON, GR-3) with 10-20 mm planform and 20-30 mm vertical accuracy (Figure S1 and Figure S2).

(4) Photogrammetric Processing

PIX 4D 4.4.10 software was utilised to produce DOM and DSM products. Each project must go through three steps of initial processing, point cloud and mesh, DSM and DOM. The camera model used for data splicing is FC6310_8.8_5472*3648 (RGB), the geographic coordinate system coordinate of images is WGS84 (EGM96 Geoid), and the output geographic coordinate system is UTMzone 47N (EGM96 Geoid). The details of the parameters used in data processing were described in the supplementary file.

(5) Error Reporting

We used the measurement results of RTK-GPS to calibrate the coordinates of UAV-SfM, and used horizontal error, vertical error and RMSE of ground control points and check points to evaluate the accuracy of UAV-SfM. In this article (Luo et al., 2020), the feasibility of using UAV-SfM in the study area from the point, line, and surface perspectives all have been evaluated and discussed. We give the error of all ground control points and check points in this study (Table S2).

2.2.2 Climate data

Climate data were obtained from a meterological station (HOBO RX3000, with five probes measuring temperature, precipitation, relative humidity, wind speed and direction (100°20′29.81″E, 36°9′8.05″N). The weather station was located in the upwind direction of Ertala sandy land in the Gonghe Basin (Figure1). The wind speed and direction data were automatically recorded by an anemometer and a 16-azimuth weathervane. The wind direction range was 0~360 ° (the north direction was set as 0 °). In this study, the meterological station recorded parameters with a five-minute interval. During the monitoring period (2019.08 - 2020.08), the average annual temperature in the study area was 3.39℃, the hottest month was August (15.48 ℃), and the coldest month was December (-11.01 ℃). The annual precipitation is 298.88 mm, mainly occurring in the period May to July (Figure 2). The wind below 6 m/s accounts for 92.75%, while wind greater than 12 m/s have a very low frequency, accounting for only 0.66%. The study area has a bimodal wind regime, and the WNW and E are the main wind direction, with a frequency of 11.93% and 12.9%, respectively. However, the wind above 6 m/s was mainly WNW, with a frequency of 51.93% (Figure 2).

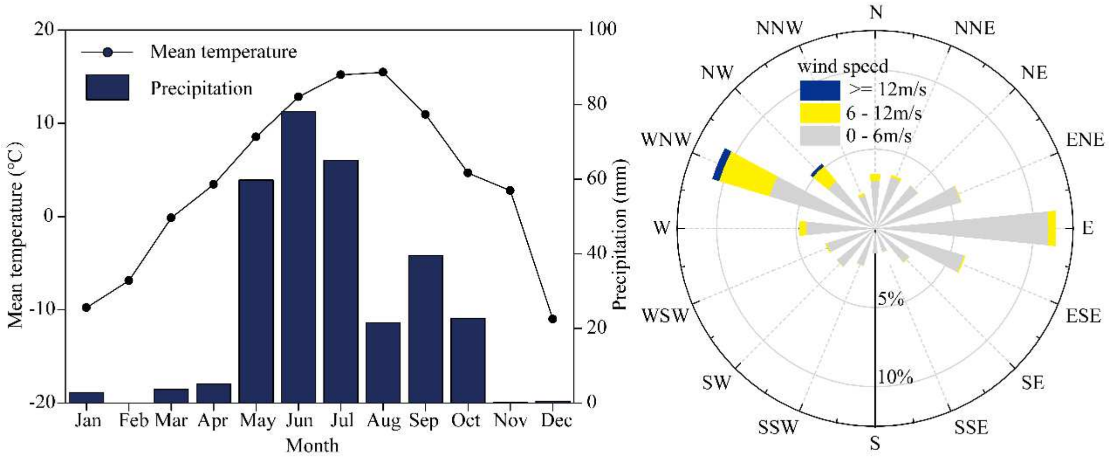

Figure 2. The mean temperature, precipitation and wind rose of the study area from August 2019 to August 2020.

2.2.3 Measurement of barchan dune celerity and morphological parameters

We obtained contour and brink information for barchan dunes based on data extraction from DOMs produced via UAV-SfM. In this work, the celerity of dunes was defined as the ratio of the distance a dune moved to its time in two adjacent monitoring periods (Sam et al., 2015). In addition, we also quantified changes in dune morphological parameters between specific monitoring periods. Figure 3a shows a schematic diagram of the dune celerity measurement approach adopted here (Zheng et al., 2022; Bristow, 2019), and figure 3b outlines the dune morphology parameters that we used (Yang et al., 2021; Merwe et al., 2022). In this paper, the derived dune morphological parameters included: dune height (H), dune length (L), the length of left horn (L_L), the length of right horn (L_R), the length of windward slope (L_W), dune width (W), and the basal area of the dune (S). Changes in these morphological parameters (ΔL, ΔH, ΔW, ΔS) between two sample periods were calculated using equations (2) to (5). Due to differences in the movement rates of the left and right horns of the dune and the dune slipface, we measure the movement of the two horns and slipface, where D_L represents the movement distance of the left horn, D_R represents the movement distance of the right horn, and D_C represents the movement distance of the slipface. The dune celerity is calculated using the following formula:

$$V_C=\frac{D_C}{\Delta t} \tag{1}$$

Where V_C represents the celerity of the dune, m/M; Δt represents the time interval, month(M).

$$\Delta L=L_1-L_2 \tag{2}$$

$$\Delta H=H_1-H_2 \tag{3}$$

$$\Delta W=W_1-W_2 \tag{4}$$

$$\Delta S=S_1-S_2 \tag{5}$$

Where L_1, H_1, W_1 and S_1 represent the dune morphology parameters of the former period, L_2, H_2, W_2 and S_2 represent the dune morphology parameters of the latter period.

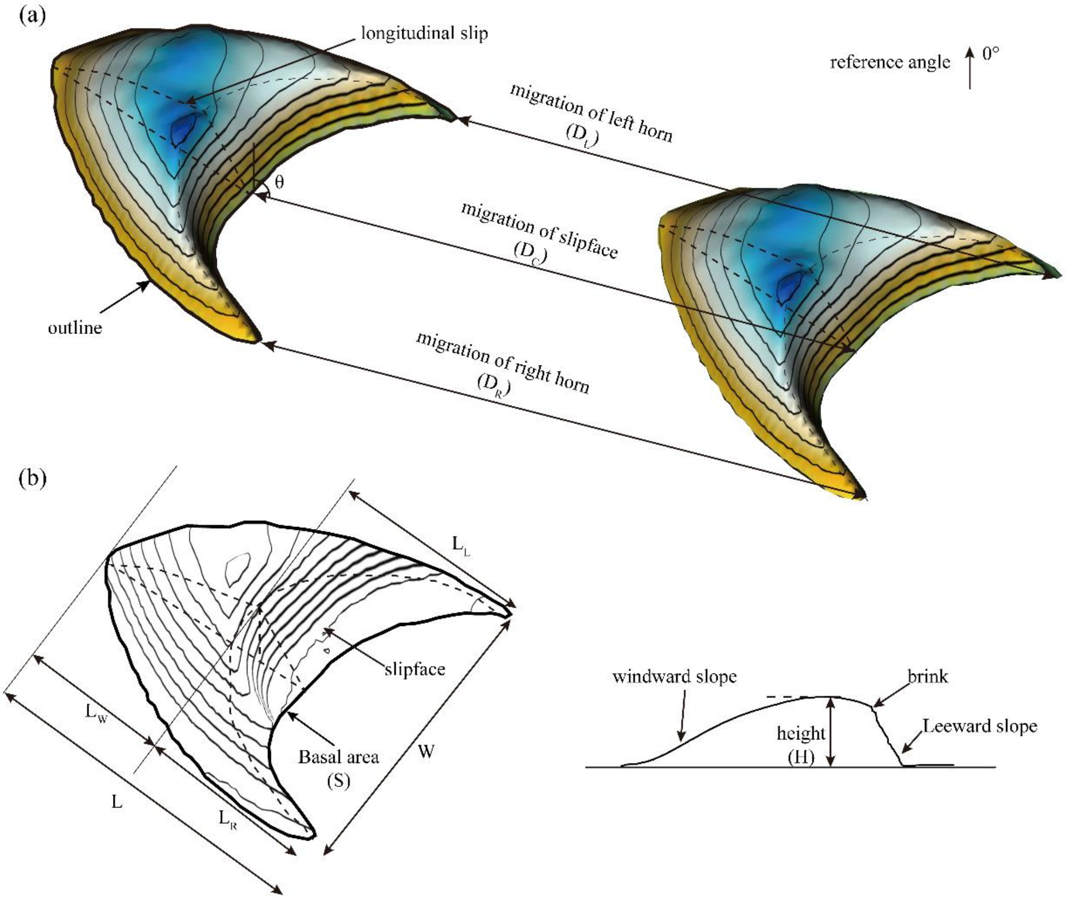

Figure 3. Schematic representation of the measurements of barchan dune celerity(a) and morphological parameters (b) used in this study.

Here, changes of erosion and accumulation were also evaluated. The net change of the dune surface, termed the erosion/accumulation depth (ΔDSM) was obtained by subtracting two elevation data sets (see eq.6)). A negative value for ΔDSM indicates net erosion, and a positive value indicates a net accumulation.

$$\Delta DSM = DSM_2 - DSM_1 \tag{6}$$

Where DSM_1 represents the DSM of the previous period, the DSM_2 represents the DSM of the latter sample period.

2.2.4 Dune deformation analysis

The difference in length between the two barchan horns is also an important component of barchan dune morphology. Here we used the L_W/W ratio (a/c, Long and Sharp, 1964), and differences in horn length to assess the asymmetry of the dunes in the study area and to monitor their dynamic changes over time.

We also used D (total planform deformation), D_a (even deformation) and D_{na} (uneven deformation) to describe the dune deformation. Total planform deformation measures the overall change in shape of the dune, considering both even and uneven deformation. The even deformation parameter is the homogeneous strain of dunes. The uneven change parameter represents the residual displacement after even transformation, meaning the amount of deformation that cannot be explained by the even deformation parameter. The calculation steps for these planform deformation parameters, based on two dune images, are as follows (Figure 4 a, c):

(1) Extract the dune outline from the DOMs for two monitoring periods, then translate the outline of the later period (t_2) to the former (1). The distance between the two was D_C, and the direction of translation for the outline is the opposite direction of dune movement in the two sample periods.

(2) Extract the location of sample points from the outline and calculate the total planform deformation. The extraction and calculation of samples points are explained in detail in Figure 4.

$$D = \| r'_i - r_i \| \tag{7}$$

Where D is the total planform deformation, m/M, r_i represents the position coordinates of the dune outline points at the earlier stage, and r'_i is the position coordinates of the dune outline points at the later stage.

(3) Calculate the uneven (D_{na}) and even (D_a) planform deformation parameters of the dune.

$$D_{na} = \sum_{i=1,2,......} \| {r'}_i^A - r_i \|$$

$$= \sum_{i=1,2,......} \sqrt{({x'}_i^A - x_i)^2 + ({y'}_i^A - y_i)^2} \tag{8}$$

$$D_a = \sum_{i=1,2,......} \| r'_i - {r'}_i^A \|$$

$$= \sum_{i=1,2,......} \sqrt{(x'_i - {x'}_i^A)^2 + (y'_i - {y'}_i^A)^2} \tag{9}$$

$${r'}_i^A = E(t, \delta_t, r_c) r'_i \tag{10}$$

where $(x_i,\ y_i)$ represents the location of sample point i at the earlier stage, and $(x'_i,\ y'_i)$ represents the location of sample point i at the later stage, $(x_i'^A,\ y_i'^A)$ represents the location that $(x'_i,\ y'_i)$ would be in if all deformation occurred along the even deformation matrix A. $E(t, \delta_t, r_c)$ represents the even transformation matrix. D_a and D_{na} are dimensionless parameters.

In this work, we use the residual elevation differences, Π(m/M, the interval of each measurement was several months so the deformation of the dune was represented by m/M here). Π represents the vertical deformation at each point on the dune (Lee et al., 2019), which directly measures the accumulation/erosion of the barchan dune.

The calculation steps of Π based on two dune images are as follows (Figure 4 b, d):

(1) Extract the elevation and coordinate location of the dune profile along the central axis of the dune in two images.

(2) Shift the later dune profile to the former, the distance of which was the D_C, the direction of which was the opposite direction of dune movement in the two periods.

(3) Calculate the vertical deformation parameter of the dune using the following formula:

$$\Pi = \frac{\eta(x+D_C,t_2)-\eta(x,t_1)}{\Delta t} \tag{11}$$

where $\eta(x+D_c,t_2)$ represents the elevation at time t_2, m; $\eta(x,t_1)$ represents the elevation at time t_1, m; Δt represents the time interval. In this study, the image of the dune taken in March 2019 (Figure 4) was taken as a reference, and the dunes in the image of the other three periods were shifted.

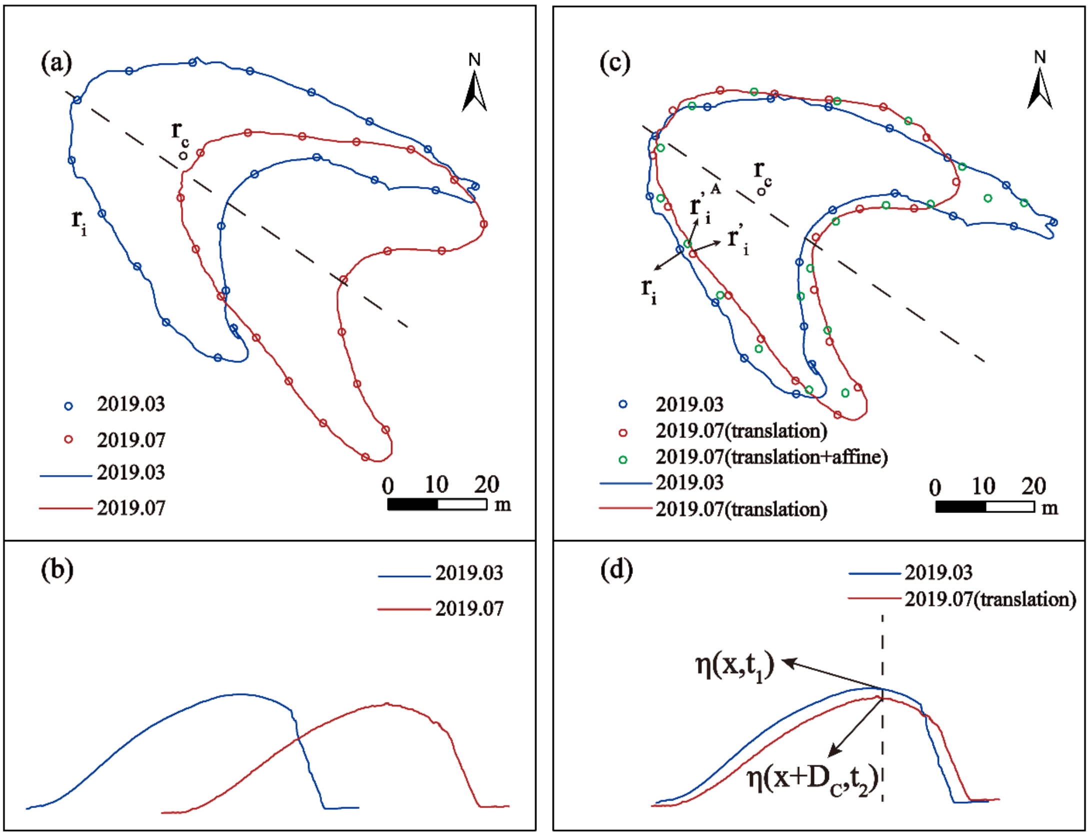

Figure 4. Definition sketch for deformation variables used here (a) and (c) show the calculation principle of planform deformation; (b) and (d) represent the calculation principle of vertical deformation. The two different coloured lines represent the dune planform outline and profile sampled at two different months, March (blue) and July (red) 2019. The lines in figure b and d represent the same profiles but with the red line (July) shifted back by the profile travel distance, D_C. The selection method for even and uneven deformation points was as follows: firstly, the position of the bottom edge of the windward slope of the dune was selected, and then the remaining

points were selected by using an equal proportion method according to the relative circumference of the dune (Modified from Lee et al., 2019).

2.2.5 Air flow and sand transport

(1) Equipment

Ultrasonic anemometer (UA) is providing a new insight into turbulent characteristics and subsequent sediment transport studies while challenges remain in field setup and post-processing (Smith et al., 2017). In this study, a calibrated two-dimensional ultrasonic anemometer (DS-2) was used in April 2019 to observe wind speed and direction on dune surface. The instrument provided an integrated measurement of wind speed and direction. The resolution of wind speed was 0.01 m/s, the range of wind speed was 0~60 m/s, the resolution of wind direction was 1°, and the observation range of wind direction was 0~360°.

(2) Survey Design and Execution

The measured height was about 5 cm from the dune surface, and the synchronous observation was adopted to obtain the surface synchronous airflow. Therefore, the observation of the near-formation airflow was only carried out on a small dune (No.2 dune) in the study area (Figure 1). The windward slope of the dune is 47.1m long, the width of the dune is 57.6 m, and the height of the dune is 3.44 m. A total of 31 UA (DS-2) were arranged to measure the airflow (Figure S3a and S3c). The measurement frequency was 0.1 HZ, and the measurement time was 20 minutes.

At the same time, a vertical step-like sand collector (see Figure S3b) was used in April 2019 to observe the sand transport flux within a height of 1 m on the surface of No. 2 dune (see Figure 1). The size of sand inlet was 0.02 m high × 0.02m wide, with a total of 50 layers. A total of 6 sand collecting instruments were set on the surface of the dune, and the sand collecting time was 10 minutes. During sand collection, the step-like sand collectors were placed in a position which faces the direction of the incoming wind flow. When sand entered the sand collector at each height, the sand was transferred from the collecting port and stored in the rear sand collecting container. Finally, the collected sand samples of each height layer were weighed and recorded with a 1/1000 electronic balance. Since the weight of the sand collected above 0.4 m was negligible, only the sand accumulation data below 0.4 m was used for calculation and analysis here. To facilitate the analysis, we convert the sediment weight into the sediment transport rate in grams per minute (g/m).

(3) Data processing

In this study, surfer13 software was used for air flow data processing. The specific processing steps were as follows. (a): The point data was interpolated into grid data. The wind speed and direction data of each point measured in the field are in text format. Firstly, the Kriging interpolation method is used in surfer software to generate grid data of wind speed and direction data. When interpolating, the variance model defaults to linear with slope of 1 and aniso of 1 and 0 respectively. The difference interval between the x and y axes is the default. The conversion function of Z values is linear. (b): Add

DSM data to the created project file as the base map of the flow field. This step also requires converting the DSM data into a grid file now. (c): Load vector files (pre-processed grid files of wind speed and direction) on the existing base map. (d): Adjust the Angle and coordinate system of the vector file. The coordinate system is polar, and the Angle 0 is set to north.

3. Results

3.1 Wind regime

The average daily wind speed in the study area was within the range of 0-10 m/s (Figure 5a-d), the average wind speed during the entirety of each monitoring period was between 2-3 m/s, and the average annual wind speed was 2.02 m/s. The average annual wind speed in Gonghe Basin is therefore slightly lower than for other deserts in China (Liu, 2018; Gu et al, 2022). In the study area, the average daily wind speed in winter and spring is significantly higher than that in other seasons. Resultant drift potential reflects the potential transport capacity of wind for sand in a region, according to the meteorological data and surface sample data collected in the study area is 5.48 m/s, and the resultant drift potential in each monitoring period is calculated based on this. During the entire monitoring period (16 months), the total resultant drift potential of the study was 166.76 VU, and the annual resultant drift potential was 125.07 VU, which is a low wind energy environment (Figure 5 h). The direction of sediment transport is 140.19°, the wind variability index is 0.63, which belongs to the medium ration. Among the three monitoring periods, the resultant drift potential of the third monitoring period is the largest, while that of the first period is smallest. It should be noted here that the resultant drift potential of the first period is one month later than the measurement time of the UAVs. The direction of synthetic sediment transport in each monitoring period is consistent, indicating that the regional synthetic wind direction is mainly WNW, and the wind direction variability is around 0.6 (Figure 5 e-h).

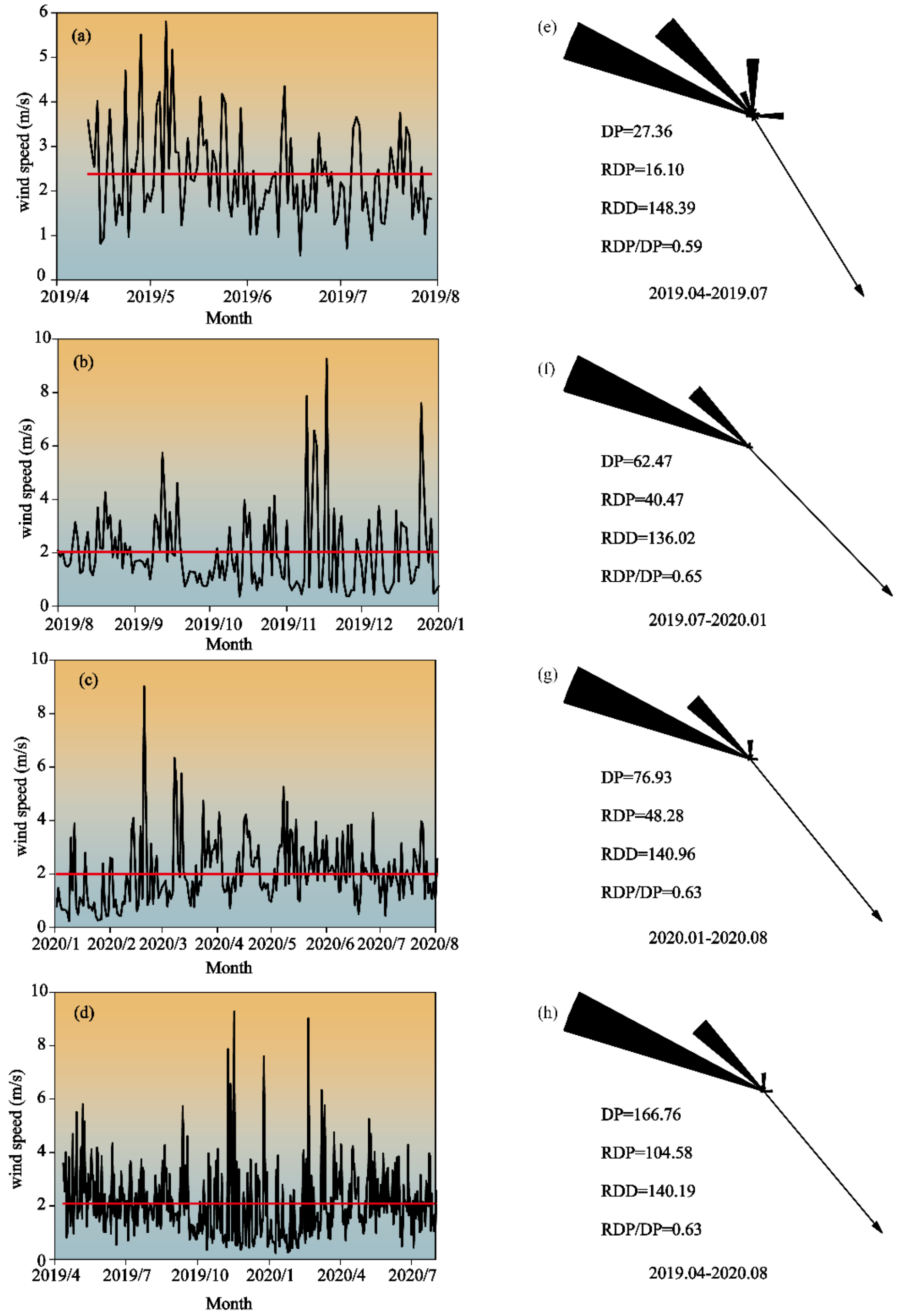

Figure 5. Daily mean wind speed and sand driving wind rose in every monitoring period. Figure (a)-(d) represent the daily mean wind speed variations in the study area, and the red line is the average wind speed in each monitoring period. Figure (e)-(h) show the resultant drift potential in each monitoring period.

3.2 Barchan dune shape

In this study area, detailed morphological parameters were generated for 16 dunes. According to the morphological classification standard (Long and Sharp, 1964), within our sample there are 2 slim types ($L_W/W<0.5$) types, 7 normal types ($0.5 \leq L_W/W<0.75$) types, 3 pudgy types ($0.75 \leq L_W/W<1$) and 4 fat types ($L_W/W>1$). Most barchan dunes in the study area were asymmetrical. Only dune No. 10 and No.14 displayed roughly equivalent (symmetrical) arms. Among the asymmetric dunes right dunes horns (except dune No. 12 and No. 15) were typically extended further than the left, occasionally even reaching 15.58 times of the length of the left horn (Table 2).

Table2. The barchan dunes morphological parameters

Dune number	H(m)	L/W	L_W/W	L_R/L_L
No.1	6.6	3.31	0.67	3.72
No.2	3.44	1.51	0.82	2.03
No.3	5.65	1.58	0.77	1.47
No.4	14.42	2.96	0.45	4.85
No.5	5.71	3.93	0.67	3.49
No.6	6.22	4.7	1.2	4.17
No.7	6.09	1.49	0.64	1.71
No.8	4.16	2.87	1.78	9.59
No.9	8.1	2.55	1.06	15.58
No.10	2.49	1.33	0.72	0.81
No.11	3.36	2.88	1.71	1.9
No.12	5.17	0.95	0.69	0.18
No.13	8.04	1.87	0.56	6.13
No.14	3.67	0.92	0.46	0.98
No.15	4.1	0.97	0.76	0.25
No.16	4.97	1.46	0.74	1.52

3.3 Barchan dune celerity

Figure 6 shows that the average celerity of all dunes in the study area was about 0.85 m/M ('m/M' = meters of movement per month) between March 2019 to August 2020. The celerity per dune was classified using the Zhu et al (1981) scheme, and fast (>10 m/yr) types accounted for the largest proportion (50%), followed by medium (5~10 m/yr, 44%), and slow (<5 m/yr, 6%). As expected, dune celerity data here exhibited the significant variability in relation to dune size, where the maximum rate was up to 10 times the minimum. For example, in July 2019, the dune celerity of No.10 (the location see Figure 1) was 2.15 m/M, and that of dune No.4 (the location see Figure 1) was 0.21 m/M. The average dune celerity between July 2019 and January 2020 was also faster than other periods, and the third measurement period (from January 2020 to August 2020) was the slowest. We also measured the celerity of left and right horns of the barchan dunes (Table S3). In the three measurement periods (2019.03~2019.07, 2020.01~2020.08 and 2019.03~2020.08), the movement of the left horns was faster that the right. In the second period (2019.07~2020.01), the movement of the right horns was faster. Figure 6 and table S3 all show that the symmetry of barchan dune have no obvious influence on the dune celerity.

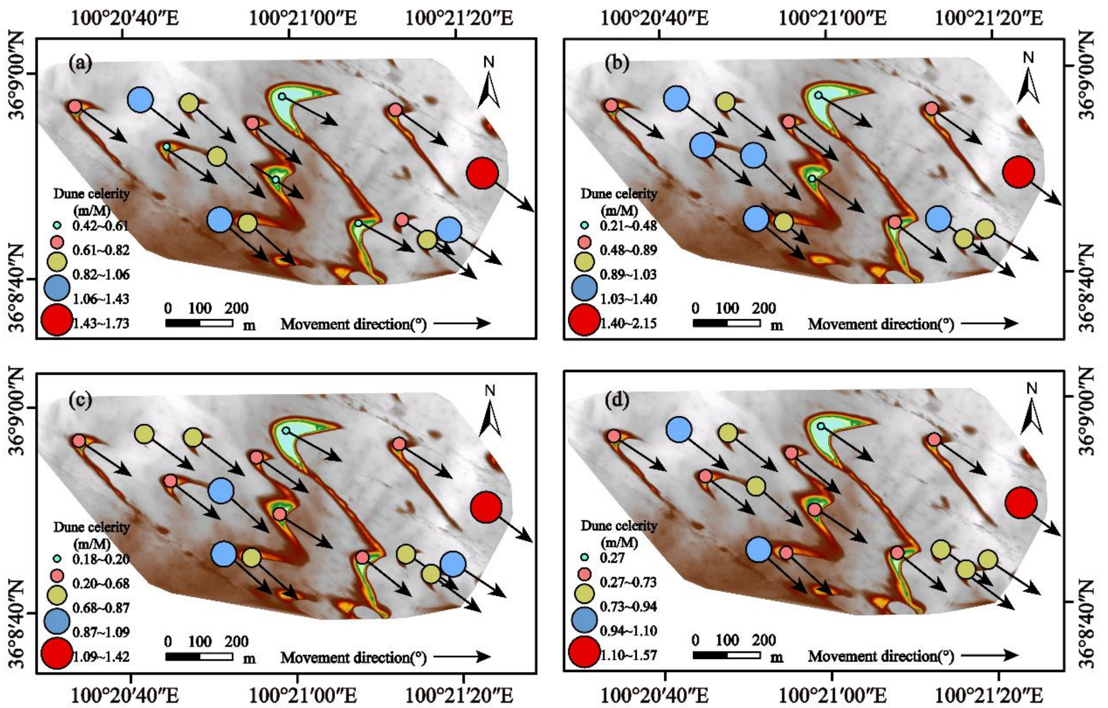

Figure 6. Maps of barchan dunes' celerity and direction. (a) The celerity and direction of dunes in 2019.03-2019.07. (b) The celerity and direction of dunes in 2019.07-2020.01. (c) The celerity and direction of dunes in 2020.01-2020.08. (d) The celerity and direction of dunes in 2019.03-2020.08. 'm/M' represents meters per month.

3.4 Vertical dune deformation

We calculated the parameter Π, which represents the vertical deformation of the dunes across our different monitoring periods (Figure 7). We observe that smaller absolute values of Π equate to lower erosion/deposition magnitude. Also, higher absolute values of Π reflect greater is the vertical deformation. The value of Π from March 2019 to August 2020 ranged from $\pm$0.3 m/M, which was a little higher than the calculations of Lee et al (2019) (±2 m/yr). We see a broad trend, whereby vertical deformation degree for smaller dunes was slightly higher than that of larger dunes but note that the correlation between these data is not strong.

Across the study region, higher accumulation and erosion was observed on the leeward slopes and the extended right horn of our dunes. The characteristics of dune erosion and accumulation in the first (2019.03~2019.07) and third periods (2020.01~2020.08) were similar; whereby windward slopes experienced relatively low levels of accumulation, and accumulation depths were typically within 0.13 m. While in the second period, the windward slope was dominated by low rates of erosion, and the erosion depth was typically within 0.10 m.

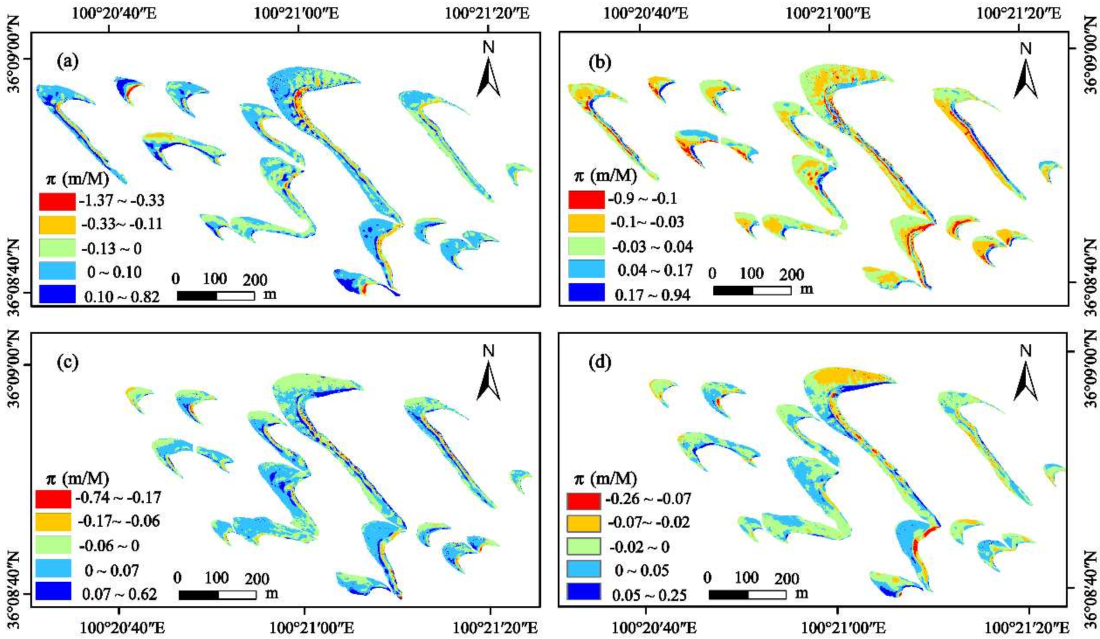

Figure 7. Distribution maps of vertical deformation of individual dune in the barchan dune field. (a)The monthly vertical deformation in 2019.03-2019.07. (b) The monthly vertical deformation in 2019.07-2020.01. (c) The monthly vertical deformation in 2020.01-2020.08. (d) The monthly vertical deformation in 2019.03-2020.08.

3.5 Planform deformation

3.5.1 Total planform deformation

During the whole monitoring period, small dunes (height < 5 m) showed a trend of shortening, widening, an increase in height, and an increase in the basal area. Large dunes (height > 5 m) showed a trend of lengthening, widening, an increase in height and an increase in the basal area (see Figure S4). Figure 8 provides a temporal and spatial summary of the distribution of the total deformation characteristics of dune outlines and brinks in our study area. These data were classified into five categories according to the natural discontinuity classification method. The total planform deformation D of the dune outlines in the study area ranges from 0 to 15 m/M. The summary value of D in the first monitoring period (Figure 8a) was significantly higher than that of the other monitoring periods (Figure 8b, c, d). Spatially, with an increase of dune scale, the value of D for dune outlines increased, and the degree of the total deformation on the windward slope was generally greater than that of the leeward slope. The degree of total planform deformation at the brink was smaller than that at the outline, but we found a consistent trend at the barchan dune scale whereby large dunes (dune height > 5 m) showed generally greater brink deformation than that at the small dunes (dune height < 5 m). The average of the former was 1.64 m/M, while the latter was 0.76 m/M. The value of total planform deformation at the brink of the large dunes even reached 11.06 m/M, commonly associated with the extended horns of asymmetric dunes.

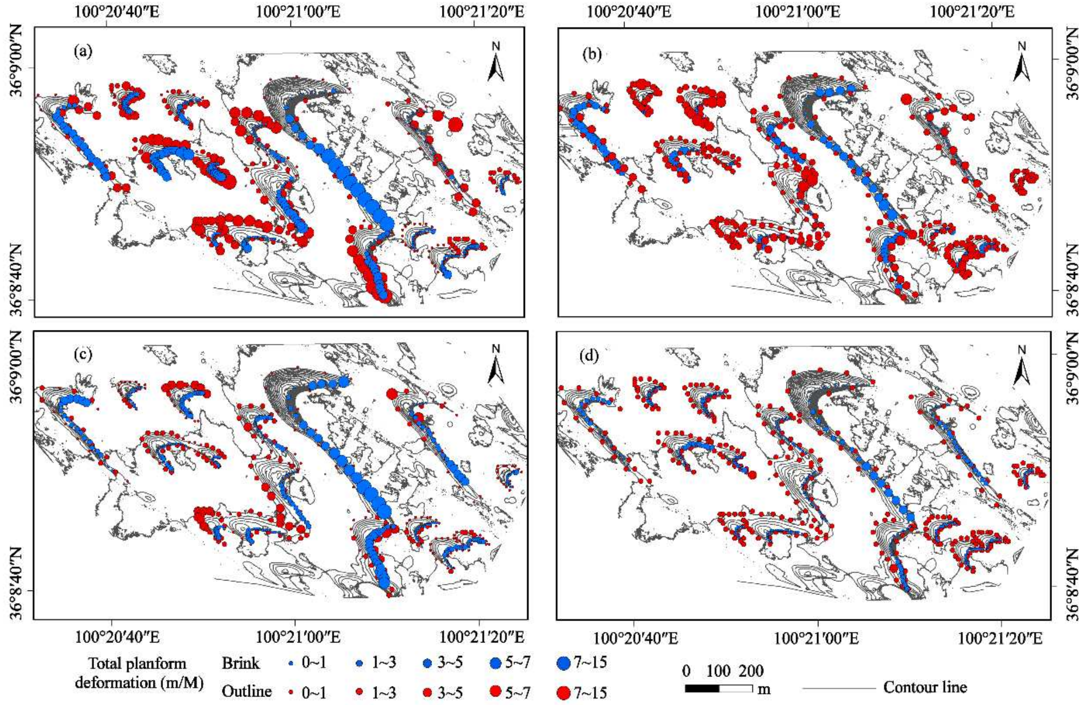

Figure 8. Temporal and spatial distribution of total planform deformation of barchan dunes. (a) The monthly total planform deformation in 2019.03-2019.07. (b) The monthly total planform deformation in 2019.07-2020.01. (c) The monthly total planform deformation in 2020.01-2020.08. (d) The monthly total planform deformation in 2019.03-2020.08.

3.5.2 Even deformation

Even deformation refers to the homogeneous strain of dunes, and, as noted above refers to the uniform (homogeneous) change in shape of the dune, where all parts of the dune are assumed to change by the same amount. However, it is difficult to directly reflect the characteristics of even planform deformation for dunes due to the large differences in D_a. Here, D_a was divided into 4 types by quartile of the maximum D_a, and the classification type and range for these are shown in figure9. The results show that D_a varied from 1.53 to 84.16 for dune outlines and was distributed from 2.07 to 107.89 for dune brinks. The even deformation of different dunes varied greatly within and between each monitoring period (Figure 9). For example, the D_a of dune No.13 for its outline was 84.16 from March 2019 to July 2019, while that of dune No.16 was only 2.48. As shown figure 9, the degree of even deformation of the 16 dunes in the study area mainly skewed towards low deformation (70.3%), followed by medium deformation (21.1%), high deformation (6.3%), and very high deformation (only 2.3%). The degree of even planform deformation in the total monitoring periods was lowest between March 2019 to August 2020 where the low deformation class accounted for more than 94%.

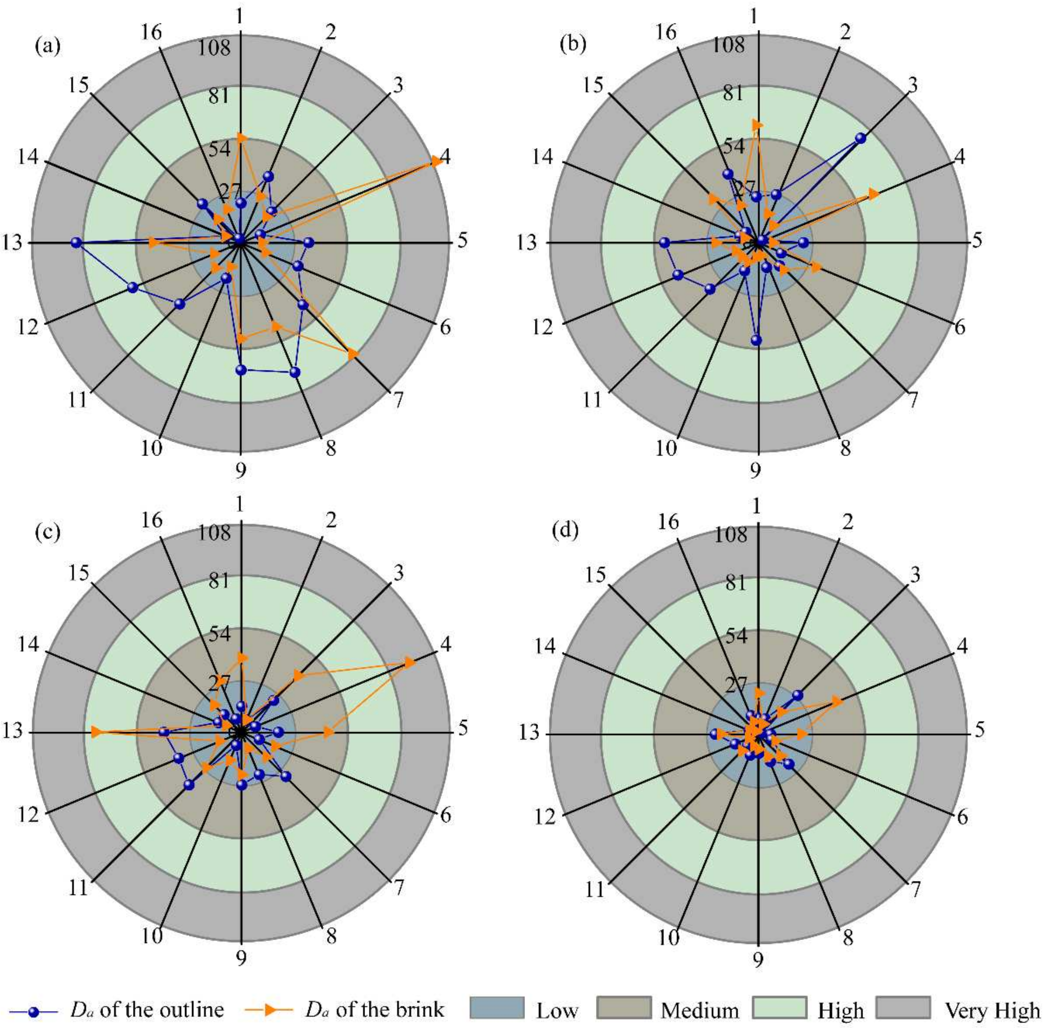

Figure 9. The value of even planform deformation of individual dune on the counter and brink (1-16 in the figure represents the number of dunes. (a) The even planform deformation in 2019.03-2019.07. (b) The even planform deformation in 2019.07-2020.01. (c) The even planform deformation in 2020.01-2020.08. (d) The even planform deformation in 2019.03-2020.08. Low (0-27), Medium (27-54), High (54-81), Very High (81-108).

3.5.3 Uneven deformation

Uneven deformation accounts for the residual deformation after even deformation calculation for dunes. The results here show that the D_{na} ranged from 3.15 to 58.67 for dune outlines and from 0.75 to 21.78 for dune brinks (Figure 10). D_{na} was less than D_a in both range and mean. The variation of D_{na} was consistent with that of total planform deformation D and even deformation D_a. The degree of uneven deformation was the lowest during the monitoring period from March 2019 to August 2020 (table 3). The mean value of D_{na} from March 2019 to August 2020 for dune outlines was 9.57, while that of dune brinks was only 2.17. D_{na} decreased over time, and the mean value of D_{na} at the dune brink was less than that at the outline in each period, which was different from D_a. D_{na} was also classified in order to facilitate the analysis of the degree of uneven deformation (Figure 10). The results show that the degree of uneven deformation was mainly low deformation (86.7%), followed by medium deformation (10.9%), and finally high deformation (2.3%). There was no very high deformation type in the uneven deformation, and the degree of uneven deformation of the dunes was lower than its even deformation. Low (0-27), Medium (27-54), High (54-81), Very High (81-108).

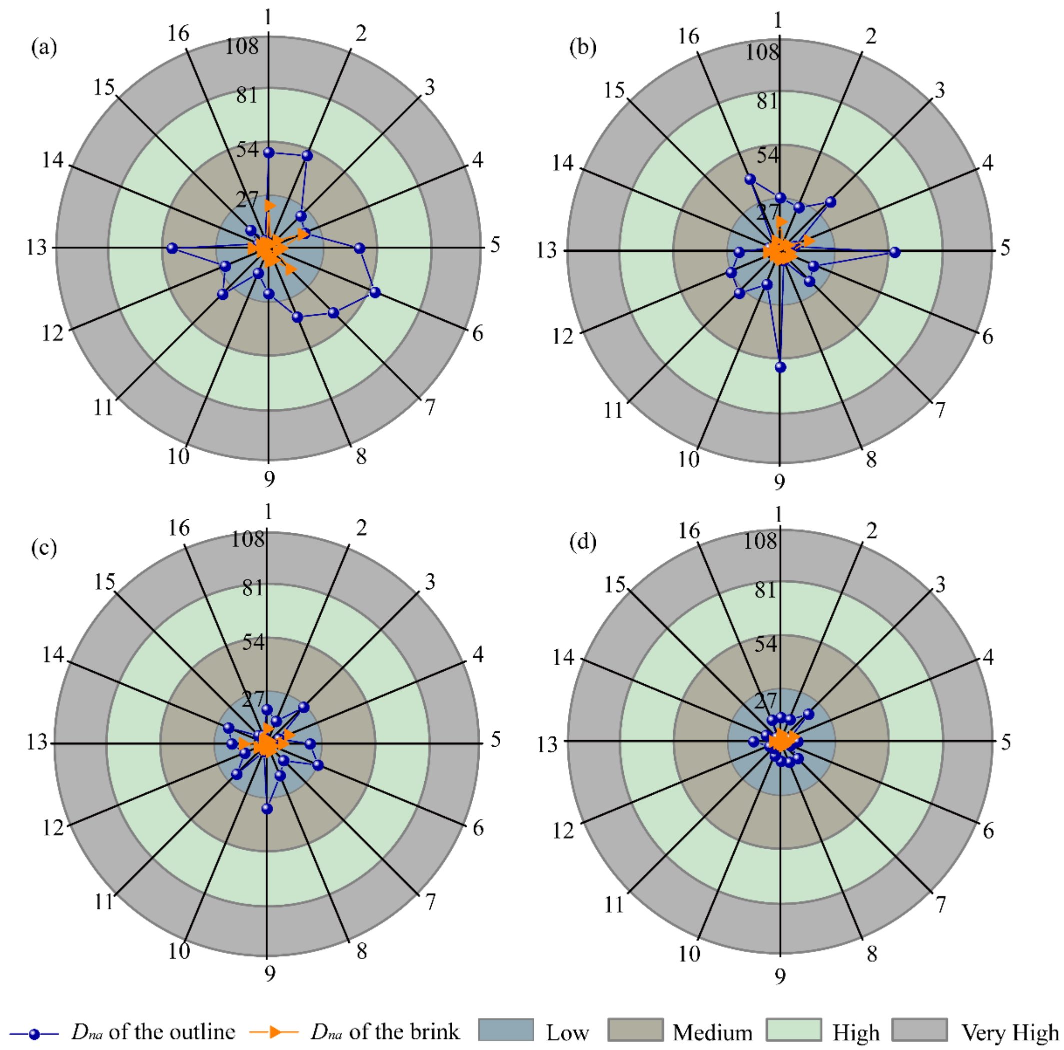

Figure 10. The value of uneven planform deformation of individual dune on the counter and brink (1-16 in the figure represents the dune number, which is link to the figure 1. (a) The uneven planform deformation in 2019.03-2019.07. (b) The uneven planform deformation in 2019.07-2020.01. (c) The uneven planform deformation in 2020.01-2020.08. (d) The uneven planform deformation in 2019.03-2020.08.

The proportions of even and uneven in the total deformation of dunes were calculated to reflect which kind of deformation the dunes tend to have. Table 3 shows that the deformation at the brink of a dune tends towards even deformation, while the deformation at the outline of the dune is roughly equal to even deformation and uneven deformation. In the deformation of a dune outline, there was little difference between even deformation and uneven deformation, where the proportion of even deformation was slightly larger (about 52%), and this proportion remained stable in each monitoring period (±2%). At the brink of the dunes, the proportion of even deformation was much larger than that of uneven deformation, with the former accounting for 81.5% and the latter 18.5%, and the proportion of the two changes greatly in each monitoring period, with a decrease of about 8% from the second monitoring period to the third monitoring period.

Table 3. The proportion of even deformation and uneven deformation of dunes

Position	Parameter	2019.03~ 2019.07	2019.07~ 2020.01	2020.01~ 2020.08	2019.03~ 2020.08
Outline	D_{na}	0.479	0.478	0.463	0.480
	D_a	0.521	0.522	0.537	0.520
Brink	D_{na}	0.195	0.238	0.154	0.153
	D_a	0.805	0.762	0.846	0.847

3.6 Three-dimensional deformation of symmetrical and asymmetrical barchan

Eastwood et al (2012) show that the dunes gradually deform in response to each sand transport wind event as deposition and erosion on the leeward surface is unlikely to be uniform. Livingstone (2003) demonstrated that the shape of the top of a dune can reflect annual climate changes, principally reflecting seasonal changes in wind orientation. In addition, results of the flume experiments also indicate that dune deformation is commonly observed (e.g. Scheltinga et al., 2020).

Figure 11 and Figure 12 show the elevation profile and deformation at the brink (from A to B) of dunes No.10 and No.4. The two horns of dune No.10 were symmetrical, and its planform and vertical deformation were also symmetrically distributed with the central axis of the dunes at the midpoint. In contrast, the two horns of dune No.4 were asymmetrical. In the vertical direction, the brink of dune No.10 was mainly eroded (the vertical deformation was negative), and, of note, the erosion was the largest observed in the first monitoring period. From the left horn of the dune No.10, the vertical deformation increased first, reaching a maximum value near the central axis of the dune No.10, and then gradually decreased. In the planform direction, the deformation of the brink of dune No.10 was mainly even deformation. Starting from the left horn of the dune, the deformation gradually decreased towards the central axis of the dune, and then gradually increased, demonstrating high deformation on the two horns and low deformation in the middle. The variation trend of vertical deformation was opposite to that of planform deformation. The brink profile on dune No.4 can also be divided into two parts, with the main part of the dune on the left and the extended part of the right horn on the right. In the vertical direction, the brink of the dune was mainly eroded. From the left horn of the dune to the right horn of the dune No.4, the vertical deformation degree gradually increased from the central axis of the dune, and gradually decreased until the middle of the elongated horn. The deformation of an asymmetric dune does not have obvious symmetry, which is different from that of a symmetric dune. In the planform direction, the brink of the dune was dominated by even deformation, and the deformation degree of the main part of the dune was significantly lower than that of the dune extension. Therefore, the deformation characteristics of the dune brink maybe closely related to its extended horn.

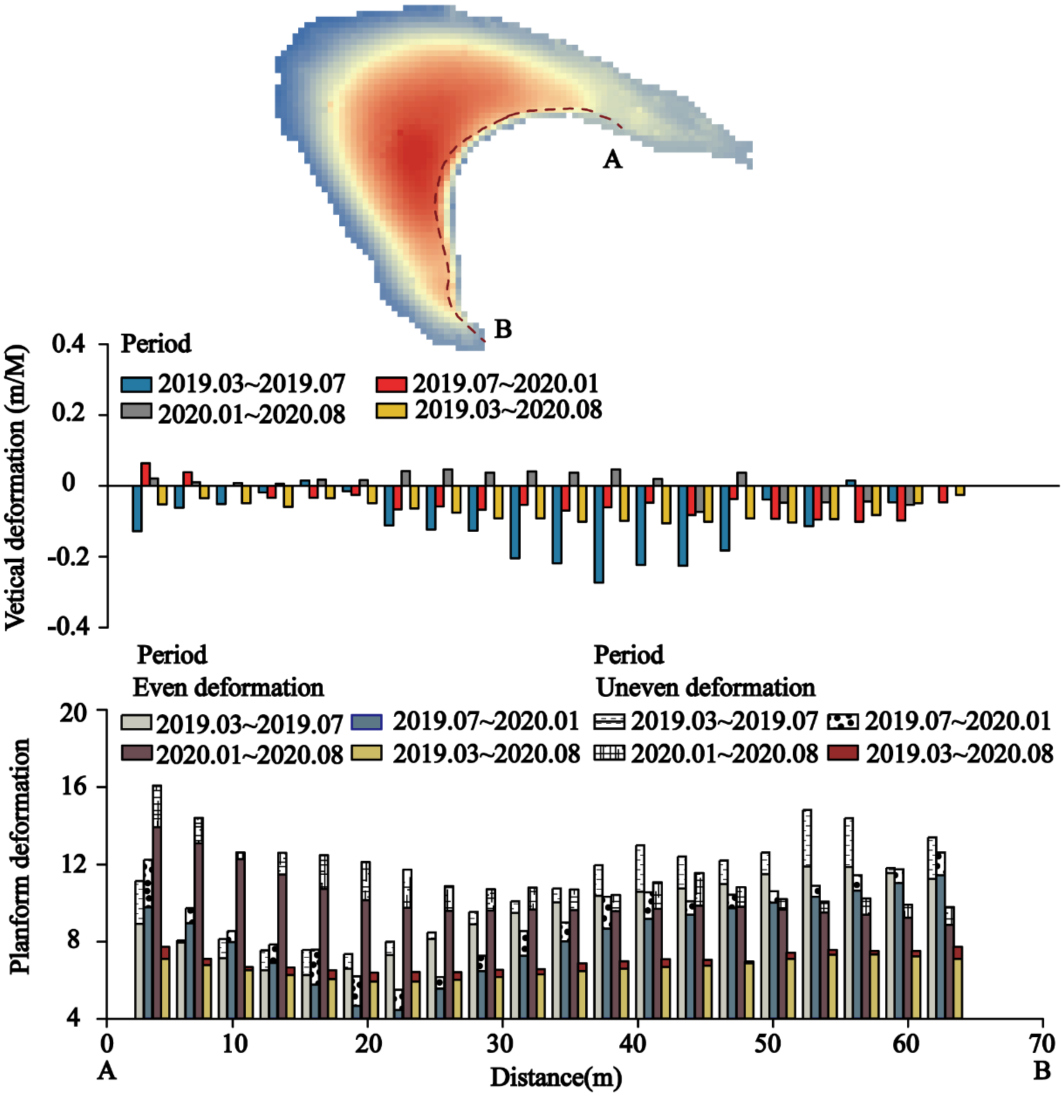

Figure 11. Three-dimensional deformation at the brink of a symmetrical barchan dune

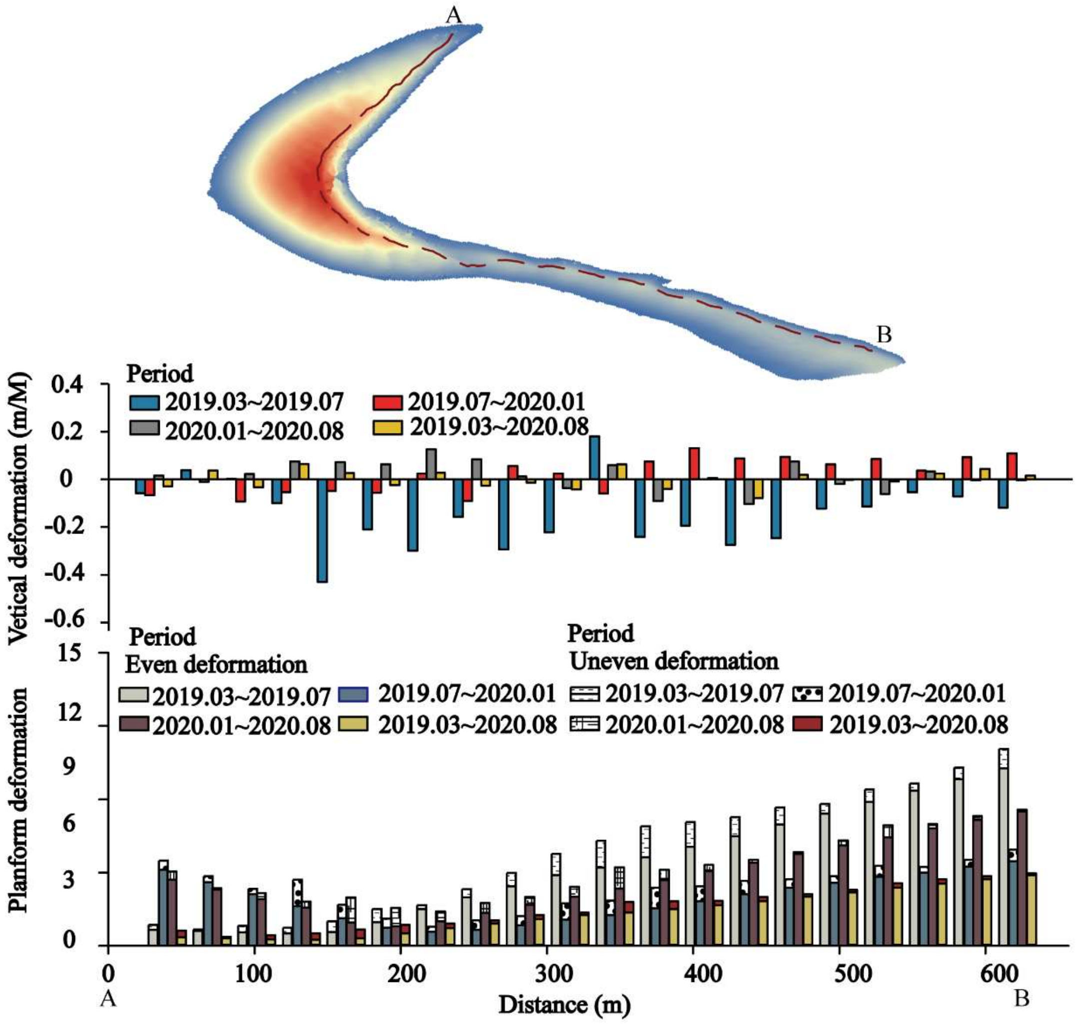

Figure 12. Three-dimensional deformation at the brink of an asymmetrical barchan dune.

3.7 Near-surface airflow and sand transport

The data of the reference point set by the upwind direction of the dune show that the airflow entered from the upwind direction of the dune at a speed of 6.26 m/s and an angle of 275°, and the flow direction was about 40° diagonally intersected with the direction of the dune (Figure 13). Then the air flow climbs along the windward slope, during which the surface air flow was divided into three branches. The first air flow passed along the axis of the barchan dune and its direction was basically unchanged before reaching the brink. The flow speed first accelerated and then decelerated, finally separated at the brink. One part of the air flow deflected to the northwest direction along the slip face, speed up the flow, the other part of the air flow generated eddy current on the slip face and the velocity slowed down, at the bottom of the slip face velocity to the lowest value, finally the flow resumed its original direction. The second air flow was deflected to the left side of the dune, its direction was relatively stable as it moved forward, but the velocity increased. This flow separated at the horn, and one stream continued in the original direction, while the other, deflected southwest and crossed the bare land of the leeward downwind to the right horn after crossing the brink. The third airflow to the right horn of the dune, moved southward along the right horn, and complex changes occurred in the process. The direction of the airflow to the north of the brink basically remained unchanged, and the airflow adjusted to the southwest on the brink to advance along the brink. The air flow on the south side of the brink was greatly deflected, and the air flow also moved along the right horn.

Within 0.4 m height from the surface of the dune, there are some differences in the sediment transport rate and direction of the 6 characteristic parts of the dune. The direction of sediment transport at the bottom of the windward slope is 275°, the direction of sediment transport at the middle and top of the windward slope has little change (281° and 279° respectively), while the direction of sediment transport at the bottom of the leeward slope is deflected (84°). The direction of sediment transport on the two horns of the dune is basically consistent with the windward slope, with the left horn being 292° and the right horn being 285°. The sediment transport rate increases first and then decreases along the windward slope. The sediment transport rate on the leeward slope (0.116 g/m, Figure 13c) is much lower than that on other parts of the dune, and the sediment transport rate on the right side (4.43 g/m, Figure 13f) of the dune is higher than that on the left side (2.87 g/m, Figure 13d), which was mainly caused by the convergence and separation of air flow. The separated air flow carried the sand grains to both sides of the left horn, and the sand transport was naturally low. The extended horn of the dune was represented by the convergence of air flow, which collected sand grains from the windward slope and falling slope to the right horn, resulting in higher sand transport. The asymmetric air flow and sediment supply may result in the asymmetrical barchan dune in the study area.

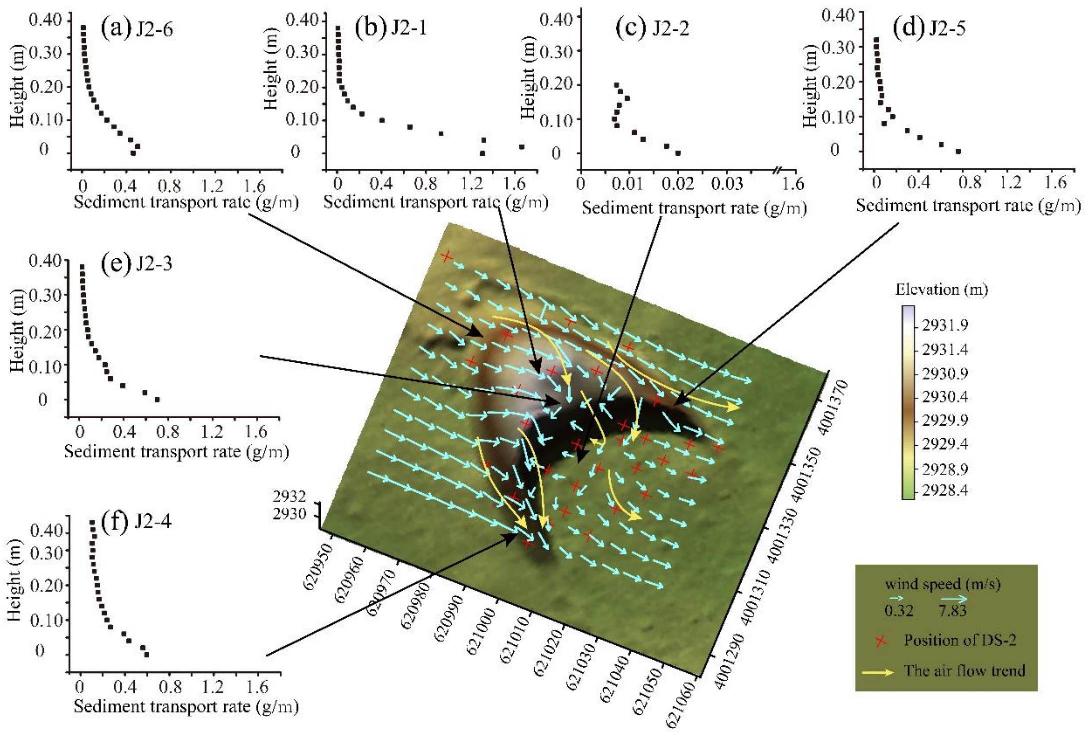

Figure 13. Characteristics of sediment transport rate and air flow on the dune surface of a barchan dune present within the studied barchan field

4. Discussion

4.1 Barchan dune morphological changes

In most cases, quantification of either vertical or volume changes for dunes via remote sensing images is challenging, but these components are necessary for the characterization of sand transport rates and associated dune morphological responses (Hugenholtz, 2010; Bryant and Baddock 2022). Vertical dune deformation has been carried out with the support of existing DEM and remote sensing data. For example, shadow effects assessed by satellite images have been used to measure dune morphological changes (Levin et al., 2004), and SRTM/ASTER GDEM data have been used to measure giant dunes (e.g. Blumberg, 2006), solve dune replacement and quantify spatial changes in sand supply (e.g. Hugenholtz and Barchyn, 2010), initial conditions for hydrodynamic simulation of dune field and validation of numerical model of dune (Jackson et al., 2011; Reitz et al., 2010). However, the limited x,y,z resolution of most global DEMs restricts the extent to which variation in vertical changes within dune fields can be derived (not least as a function of time), especially for small isolated dunes at the year/sub-year timescale.

In this work, in addition to derivation of deformation metrics, vertical variation for isolated dunes was analysed using DSM data produced by UAV-SfM on a monthly scale. Calculation was derived by direct subtract of paired DSM images without translation, which adds to our understanding of vertical deformation of the dunes discussed above by allowing metrics that more closely align with existing studies. Figure 14 summarises the respective rate of erosion and accumulation. The rate of erosion and accumulation was between ± 0.5 m/M on the windward slope and the leeward slope. In the second monitoring period, both dune erosion rate and erosion area were significantly higher than those in the other three monitoring periods. The dune erosion and accumulation rate in the fourth period were the lowest at 0.4 m/M. Only the central leeward slopes in the first two monitoring periods had a high accumulation rate, with a monthly accumulation depth of more than 0.5 m.

These data provide several insights that augment the deformation data analysis above. Firstly, the amount of vertical deformation is obviously much smaller than the amount of direct erosion/accumulation. This is because the vertical deformation removes the redundant deformation caused by the displacement of the dune. Secondly, the direct erosion and accumulation amount reflects the simple erosion and accumulation law for different parts of the dunes. The windward slopes mainly erode, and the leeward slopes mainly accumulate. However, we note that the erosion and accumulation rates for the windward and leeward slopes of the dunes were different in each of the monitoring periods, and sometimes, even opposite. Therefore, we feel that the vertical deformation metrics calculated in this paper are better able to reflect the real rates of dune deformation at appropriate space/time scales.

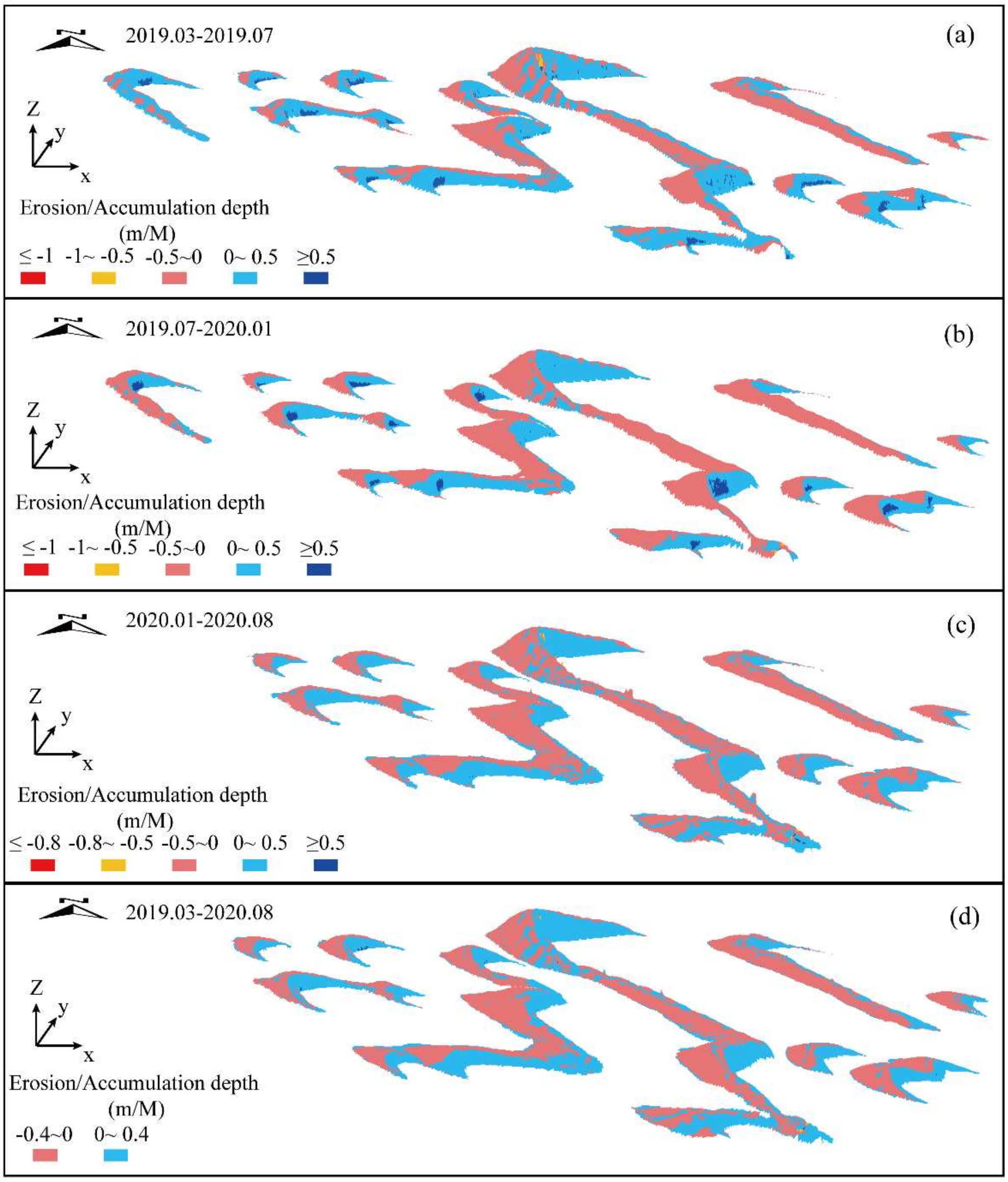

Figure 14. Characteristics of barchan dune surface erosion and accumulation in different monitoring periods. a: the erosion and accumulation of barchan dunes in 2019.03-2019.07; b: the erosion and accumulation of barchan dunes in 2019.07-2020.01; c: the erosion and accumulation of barchan dunes in 2020.01-2020.08; d: the erosion and accumulation of barchan dunes in 2019.03-2020.08. Negative values indicate erosion, positive values indicate accumulation. The units are meters per month.

4.2 Factors affecting dune celerity and deformation

The factors influencing the formation and morphology of dunes are complex (Gifford et al., 1979), and include the wind intensity, wind direction and duration; the nature, extent, and rate of erosion at the sediment source; distance from the source; grain size; underlying and surrounding topography; the amount and type of vegetation (Gillette and Chen, 2001; Duran et al., 2010; Baddock et al., 2011; Hamdan et al., 2016). It must be emphasized that because of the flat underlying terrain, sparse to zero vegetation, smooth bed surface and low rainfall we focus specifically on the impacts of sand supply, vegetation, and airflow transport.

4.2.1 Sand supply

Dunes of different heights have different shapes, thus, there should exist (at least) a typical length scale in the mechanisms leading to the dune propagation because the dunes cannot develop infinitely. Where able, barchan dunes can or will reach an equilibrium state (Narteau et al, 2009; Gao et al., 2015). The equilibrium state refers to a constant interaction occurs between shape, flow, and sand delivery/transport and produces an equilibrium three-dimensional shape which constantly adjusts to maintain a 'perfect' aerodynamic (Hesp and Hastings, 1998). And one of the most important factors in determining that state and, by inference the dune height, is the sand supply (Gunn et al, 2022). As the dune develops, more sand will be transported to the top of the dune, increasing its height until it reaches an equilibrium state under the constant interaction of morphology, wind flow and sediment transport (Hesp and Hastings,1998).

In this paper, the height of 16 dunes in the study area was predicted according to the height/width ratio formula of dune equilibrium state proposed by Hesp and Hastings (1998) and Andreotti et al (2002), and the results are shown in figure 15. The height of 13 of 16 dunes was lower than the predicted height, and only dune NO.6, NO.8 and NO.11 met or exceeded the predicted height. It was initially believed that the dunes in the study area have not reached an equilibrium state, and that the dune heights might continue to develop further. However, in charting dune movement and change in this paper (2019.03~2019.07, 2019.07~2020.01, 2020.01~2020.08), both shape and size of 16 dunes changed irregularly with time, including periods of expansion and shrinking, without showing a significant trend towards further enlargement (Table 4). In this study area, the sand supply limited by vegetation, and sufficient sand is not always available to ensure the continuous increase in size of the sand dune, which accounts for vertical and horizontal morphological deformation over time. We will discuss the influence of vegetation on the supply of sand sources in the next section to further reveal the influence of vegetation on the morphologic dynamics of sand dunes in the study area. Studies have shown that dunes may grow indefinitely in principle, but growth depends on morphology, slows with increasing size, and may ultimately be limited by sand supply (Gunn et al, 2022). Even when sand supply is low, sand dunes may become smaller over time (Yang et al, 2019). Here we see that the size of smaller dunes in the study area decreased while that of large dunes increases. Given that the sand transport flux of a barchan dune is proportional to its width (Kroy et al, 2005), it is likely that under conditions of sand source limitation, small dunes in the study area may provide a sand source for the larger dunes.

An evaluation of sand-supply is considered here in both qualitative and quantitative ways. Qualitative analyses mainly consider three aspects (i) sediment supply, (ii) wind transportation and (iii) sediment availability. The sediment supply in Gonghe Basin can also be divided into two components, internally derived sand and externally derived sand (Figure 1). The external sand supply for the Gonghe Basin is mainly derived from the Qaidam Basin, but this supply type is very limited due to topographic obstruction via mountain ranges (see figure1). Therefore, the sand source in this basin is expected to be dominated by internal sediment stores associated with fluvial and lacustrine strata deposited in the early Quaternary (Xu et al., 1982), such as Shazhuyu River, Dalianhai et al (Liu, 2018). Any internal sediment supply from upwind dry rivers and lake basins is deemed to be insufficient. A large number of course particles are distributed on the surface of the inter dune area, also reflected the restricted availability of sediment in this area. Based on field monitoring via a local weather station, the annual sand drift potential (DP) in the study area was calculated as 125.07 VU, which belongs to low energy environment, much lower than that of Aaidam Basin (199~328 VU) (Bao et al., 2015) and Tengger Desert (358.7 VU) (Zhang et al., 2008), which suggests that the sand carrying capacity is limited due to the relatively low wind energy in Gonghe Basin. Therefore, we qualitatively suggest that the Gonghe Basin is sand-supply limited. To further quantify the sand supply magnitude, we use the coefficient C proposed by Gillette and Chen (2001) to measure the degree of sand-supply to characterize the basin's sand source limitation. According to the classification given by Gillette and Chen (2001), the regional sand source is limited when the value is less than 3.2. The closer the value gets to 0, the more constrained it is. The value of C of the study area is 0.146, which confirms that the sand-supply here is indeed restricted.

Studies have shown that the appearance of a dune also depends on the amount of sand available for transport (Mckee, 1979; Narteau et al, 2009; Gao et al, 2015; Lv et al, 2018; Yang et al, 2019). According to the calculations presented here, the vertical deformation extent for the extending right horns of dunes was obviously higher than that of other parts, and especially we saw that the erosion and accumulation changes for the dune brinks were very large. At the same time, the planform deformation along the brink of the elongated horn was also high, and this was especially the case when an increase of dune scale led to increased deformation.

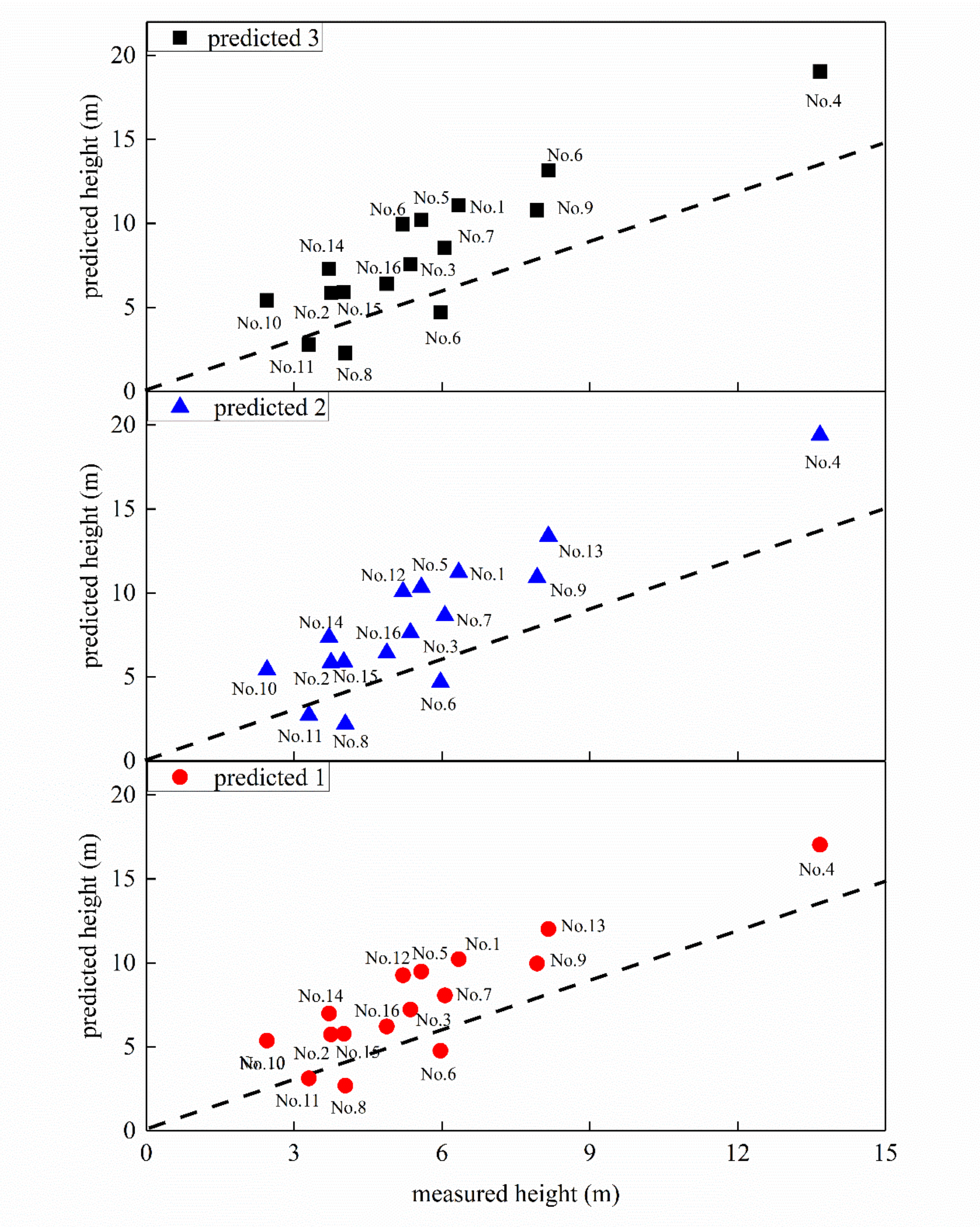

Figure 15. A comparison between the measured height and the predicted height of the barchans in the study area. (The dashed gray line indicates that the actual measured height is the same as the predicted height) The predicted height 1 using the equation of Hesp and Hastings (1998)：H=L/2*0.194, where s slope angle of 11 ° is taken as a typical average value for the side slopes of a barchan. The predicted height 2 using the equation of Andreotti et al (2002), W=8.8+8.6H. The predicted height 3 using the equation of Hesp and Hastings (1998)：W=8.82H+7.65, the data for this fitting formula is derived from Finkel (1959), Hastenrath (1967;1987), Khalaf and Al-Ajmi (1993).

Table 4. Dune morphology changes in the whole monitoring period

Dune code	ΔL/m	ΔW/m	ΔH/m	ΔS/m^2

1	9.82	-7.18	-0.11	-86.41
2	-23.23	1.5	0.06	-409.24
3	-11.32	-1.34	-0.27	-116.09
4	-20.05	-1.77	-0.46	-33.15
5	-8.41	-1.26	0.06	185.75
6	-39.91	5.8	-0.12	1020.09
7	1.93	1.78	0.09	-66.35
8	1.9	5.93	-0.13	-436.52
9	-14.18	2.28	0.38	709.44
10	-1.58	-6.82	-0.1	-240.04
11	4.54	6.14	0.46	808.08
12	7.21	-2.49	-0.19	2053.18
13	-24.73	4.88	-6.34	3634.7
14	22.58	-3.44	0.15	51.18
15	30.54	7.22	-0.34	-86.41
16	4.76	3.6	1.06	-409.24

4.2.2 Vegetation and barchan dunes celerity

Vegetation affects sand supply, sand availability decreases as vegetation cover increases, further reducing the transport rate. Vegetation is expected to trap wind-blown sediment and inhibit movement of wind-blown sediment (Kuriyama et al., 2005). The results of laboratory experiments and field measurements show that vegetation reduces the movement of surface sediments, and an area with 15% vegetation coverage can reduce the sediment transport rate by 99%. (Lancaster and Baas, 1998). The vegetation coverage in the study area is between 0.15-0.45 (Shao et al., 2021), which belongs to the low-medium coverage type, can effectively reduce the sediment transport rate and limit the supply of downwind sand sources.

On isolated dunes with limited sand supply, mobility is more sensitive to changes in vegetation cover. Compared with vegetated dunes, the near-surface wind speed and shear stress on bare dunes increased significantly, and the surface activity varied by three times (Wiggs et al., 1994). On the interdune and lower slopes, sediment movement was mainly limited by wind energy, while on the dune top and higher slopes it was mainly controlled by vegetation cover (Wiggs et al., 1995). The stable morphology of the dune is determined by the ratio of the deposition rate of the sliding surface to the deposition tolerance of vegetation. Due to the fixed sediment tolerance, the sliding surface of large slow-moving dunes has a low sedimentation rate and will freeze once vegetation is introduced. Relatively small, fast dunes have a high slip deposition rate, are easy to evolve into other forms, and often collide during stabilization (Barchyn et al., 2012). Vegetation in the interdune also plays an important role in dune mobility. An increase in downwind plant density leads to an increase in vegetation-induced morphological resistance, which leads to a decrease in dune mobility (Lee et al., 2019). The Orthomosaic of the study area showed the vegetation cover in spring in the dune field (Figure 16). The vegetation of the dune field in the study area mainly grows in the interdune, and then scattered in the foot of the windward slope of the large dune, so the dune surface activity is relatively active.

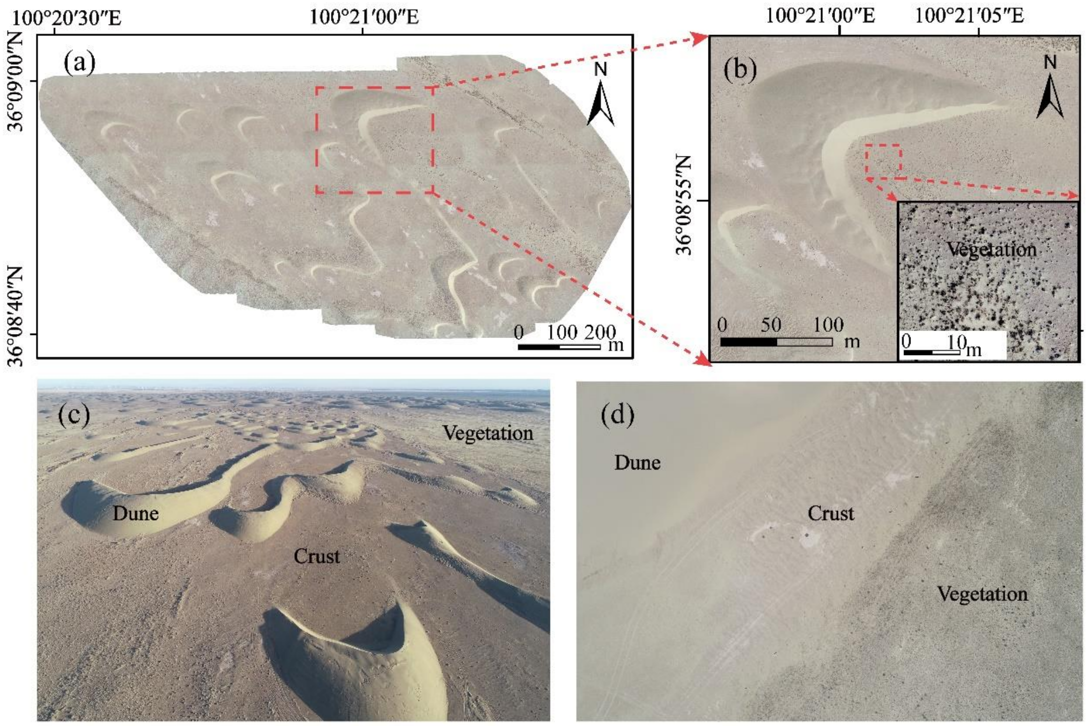

Figure 16. The vegetation cover and bed conditions in the barchan dune field. (a) The orthomosaic of the barchan dune field. (b) Local enlarged view of sand dunes and vegetation cover. (c) and (d) are the oblique photographic image of the dune field which show the bed condition and vegetation cover in the study area.

4.2.3 Sand transport and dune morphodynamics at high altitude

Wind shapes the morphology of dunes and influences their migration, playing a critical important role in their development and evolution (Bagnold, 1941; Wu, 2003; Hesp et al, 2007). The shape of the dune crest positively reflects the natural climate changes from year to year (Livingstone, 2003). Dune morphology is also strongly influenced by complex seasonal variations in wind direction. Air flow field and sediment transport rate play important roles in understanding the formation and evolution of aeolian bedforms on the microcosmic level. Historically, the relationship between dune morphology and wind regime has been used to represent morphological changes of dunes at relatively large scales (Yang et al., 2011). At the dune scale, the interaction between topography and air flow as well as air flow and sediment transport process largely determine its morphological evolution (Vandijk et al., 1999), especially regarding dune asymmetry (Bagnold, 1941; Rim, 1958; Lancaster, 1982). Some field experiments have identified complex, topographically-induced flow structures including flow stagnation downwind of the dune toe, compressed and accelerated flow on the stoss slope, detachment and flow expansion at the crest, recirculation or deflection in the lee, and downwind flow recovery (Smith et al., 2017).

The surface airflow has an important effect on dune migration. The average annual dune movement rate measured in Gonghe Basin is 10.2 m/yr, which is relatively low.

Aerodynamic resistance is proportional to air density, and extreme temperatures will lead to significant differences in wind transport capacity, so temperature and air density may be related to unique aeolian deposition patterns (Smith, 1966; Selby et al.,1974). Extensive measurements and wind tunnel experiments by many scholars show that the air flow pattern on the windward slope is mostly similar, and the air flow will converge and accelerate during its ascent along the windward slope of the dune, and the speed lines from the foot of the windward slope to the top of the windward slope will meet more and more densely (Wiggs et al., 1996; Dong et al., 2017). However, the morphological change of the part will affect the near-surface air flow along the windward slope, and the air flow will converge at the bulge and diverge at the top of the dune with relatively flat slope (Wu et al., 2011;). On the leeward side of dune, the airflow structure evolves from airflow diffusion with instantaneous airflow dispersion, and then completes airflow separation and re-attachment (Walker and Nickling, 2002; Baddock et al., 2011; Qian et al., 2021). At high altitudes, for a given volume flow, a lower air density produces a higher threshold frictional wind speed (Han et al., 2015). According to the existing research results, the altitude varies from 1140 meters to 5076 meters, and the air density changes from 1.074 to 0.676 kg • m^{-3} (Han et al., 2015). Taking the parameter of the study area (Che et al., 2021) as an example, the frictional wind speed at 3 meters of the two is 4.79 and 6.04 m/s, respectively. The air density in the study area is 0.862 kg×m^{-3}, and the frictional wind speed at 3 meters is 5.48 m/s. Therefore, the increase of altitude in the study area reduces the sediment transport by increasing the starting wind speed.

An increase in altitude also results in a corresponding increase in the rate and height of saltation. The results of wind tunnel experiments show that when the wind speed exceeds 10 m, most of the sand particles move at 10-14 cm in the altitude layer at low air density, and 6-8 cm at high expired density (Han et al., 2015). The results of sediment accumulation in this study show that 4-6 cm of sand accounts for about 30% of the total sediment transport within 2-40 cm height, and 76% to 91% of the sand saltation within 2-14 cm. Of course, the saltation height is also highly related to the type of bed surface. Even at high altitudes, there are significant differences in bed/sand availability by area. For example, Kumukuri Desert, the most distributed modern desert in the world, has continuous distribution of sand dunes on the surface and abundant sand supply, which is a typical erodible bed with high sand availability (Li, 1992). On the southeastern edge of Qaidam Basin, that is, around Qarhan Salt Lake, because the surface is mostly salt crust, there are many non-erodible beds with low sand availability (Xu et al., 2017). There are many lakes and river channels in Qinghai-Tibet Plateau, and some climbing dunes are distributed on floodplains, river terraces and hillsides, among which floodplains are erodible beds, and hillsides are mostly non-erodible beds, while river stages are between completely erodible and completely non-erodible. The bed in this study area is crust as well as grassland (Figure 16 c and d), which is of low sand availability type, and many isolated dunes are deposited on the surface which is difficult to erode. Therefore, low air density at high altitude may be a major factor hindering dune migration in the study area.

The aeolian sand flow has great influence on the shape of dune. The agent-based model indicates that both the degree of overlap between the upwind dune and downwind dune and the size of the adjacent dunes will influence the interaction (Genois et al., 2013). Different combinations of overlapping degree and dune size will create different results, such as merging, exchanging and generating a new dune. However, the latter two results have not been observed in this study due to the observation duration of the study, only the merging phenomenon of two arms of adjacent dunes caused by interaction between dunes is analysed here. Studies show that when there are other dunes near the independent dune, an acceleration zone will be generated between the two dunes, and the air flow on both sides of the horns is asymmetric (Bristow et al., 2018), thus changing the morphology of the horn of the dune. The extended horn received more sand based on the fact that the flux ejected by the horns is saturated or close to saturation (Sauermann et al., 2000; Elbelrhiti, 2012).

4.2.4 Asymmetry barchans and barchan-seif dunes

As shown in Table 2, there are both symmetric and asymmetric barchan dunes in the study area, with both left horns extension and right horns extension, and their main control factors are different. Lv et al (2016) put forward that expectation-maximization algorithm to fit the flux orientation distribution with a Gaussian mixture model can help us to identify the prevailing and secondary winds. Figure 17 shows the distribution of the wind direction. Thick arrow represents the stronger wind, thin arrow represents the gentler wind. The red line in the figure 17 b show the bimodal distribution of the wind regime in the study area with symmetric and asymmetric barchan dunes. The main wind comes from WNW (298°),with a weight of 0.79, and the secondary wind comes from ENE (71°), with a weight of 0.21. the ratio of the weights of the two winds is close to 4,u and the angle between the two winds is 227°. The direction of all barchan dunes is consistent with the prevailing wind, indicating that they are formed under the action of stronger wind. The data in the figure 17 suggest that the horns of large barchans extend farther on the side farthest from the gentler wind, whereas the limb closest to the gentler wind is eroded, which is consistent with the evolution model of seif dune proposed by Tsoar (1984).

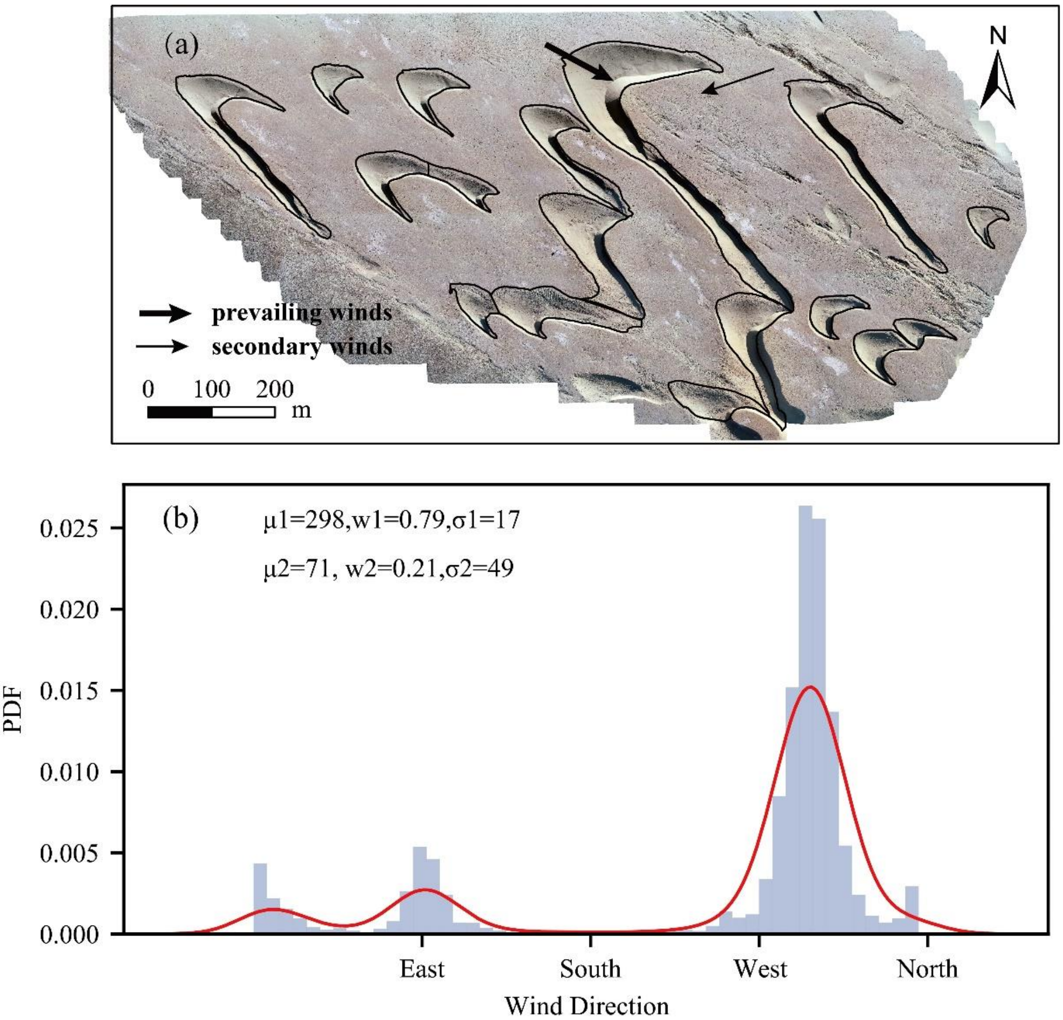

Figure17. Figure 17. wind regime characteristics in areas with symmetric and asymmetric barchan dunes. (a) The prevailing winds and secondary wind in the study area. (b) The wind direction distribution during the period from August 2019 to August 2020 based on the 5 minute-interval data. For the dominant wind direction 1 and 2, the μ orientation (north=0°), w weight (ratio of the frequency of the strongest of the two dominant winds to the frequency of the gentler dominant wind), (the standard deviation of the wind orientation), PDF proportion of the total number of winds recorded.

Asymmetric barchan dunes caused by wind conditions will show the same extension of horns (Tsoar and Parteli, 2016), which is obviously inconsistent with the study area. In the study area, the right horn of large dunes extends, while that of small dunes is different, which shows that wind condition is important to the extension of large sand dunes, while the effect on the extension of small sand dunes is secondary. The impact of collision and inflow asymmetry on the wing elongation of small dunes is more significant. It can be found that only two dunes (No.12 and No.15) have left horn extensions, whose right horn/left horn values are 0.18 for the former and 0.25 for the latter (Table 2). These two dunes are not isolated dunes, but merge with other dunes. There are five modes of interaction between dunes, namely chasing, merging, exchange, fragmentation-chasing and fragmentation-exchange (Assis and Franklin, 2021). In the study area, dune No.11 and No.12 have collided and presented a merging mode, with the left horn of the former intersecting with the right side of the windward slope of the latter, which means that the wake of the former will disturb the latter and even absorb part of the sand, and the latter may not supply enough sand, thus preventing the extension of its right horn. Although dune No.15 and No.16 also showed a merging pattern, they remained parallel downwind, sharing a horn, so that the right horn had significantly more sediment supply than the left horn. More sediment supply would prevent erosion and downwind movement of the dune horn, so the horn with less sand supply would extend more than the horn with more sand supply (Tsoar and Parteli, 2016). The elongation of a horn may depend on the shape of the dune itself (Tsoar and Parteli, 2016). The symmetry barchan dunes (No10, No.14) and that with left horn extension tend to be short and fat, while the barchan dunes with right horn extension tend to be tall and thin.

Seif dunes are a type of linear dunes that grow in unvegetated areas, form under bidirectional wind conditions, are parallel to the dominant wind direction, and have a meandering shape and sharp crest (Tsoar, 1983; Parteli et al., 2009; Tsoar and Parteli, 2016; Pang et al., 2020). The elongated right horns of large barchan dunes (No.1, No 4, No 5, No 6) in the study area has slightly meandering shape, sharp crest, and with continuous extension, so these asymmetrical barchan dunes should belong to the barchan-seif dune. By contrast, some asymmetrical barchan dunes with elongated right horn in the study area, like other symmetrical and asymmetrical barchan dunes with elongated left horn, still belong to asymmetric barchan dunes, not seif dunes. However, the mechanism of which dunes will extend into seif dunes in the study area is still unknown, and we need to follow up the morphodynamics characteristics and processes of dunes with longer time series to further explore.

5 Conclusion

In this paper, 16 isolated symmetric/asymmetric barchan dunes distributed in Ertala, Gonghe Basin were monitored using UAV-SfM to obtain the 4 high-resolution DOM and DSM. Celerity, vertical deformation, and planform deformation (total deformation, even deformation and uneven deformation) were detected based the DOM and DSM data. We qualitied the morphodynamic characteristics of symmetry and asymmetry of barchan dunes, and analyzed the influences of sand supply, vegetation and high-altitude on barchan dunes celerity and deformation. Combining the field monitoring of dune surface airflow and the collected wind data, the controlling factors of asymmetric dune evolution are discussed. During the monitoring, we found that the scale and development process of large barchan dunes will be hindered because of the low sand supply conditions and dense vegetation distribution in the study area, which is located at a high altitude. Before the size of the dune reaches the equilibrium state, the degree of vertical deformation is large, and the dune increases continuously through accretion, the size increases, and the shape changes dramatically. When the dune reaches the equilibrium state, the shape of the dune, the air flow and the sand transport interact with each other, and the shape is adjusted to maintain the aerodynamic equilibrium state. Even under the influence of external conditions, one horn of the dune gradually extends, and finally reaches the "equilibrium state".

In summary, we obtained the following insights on the morphological dynamics and characteristics of symmetric/asymmetric barchan dunes from our study: (i) barchan dune celerity is related to the dune size, but the symmetry of barchan dune has no obvious influence celerity; (ii) the deformation of the elongated arm of a barchan dune is more obvious, and symmetry may therefore play an important role in rates and extent of deformation; (iii) observed deformation at the brink of a barchan dune tends towards "even" compared with that of the outline; (iv) the sand supply, vegetation and airflow at high-altitude all influence the celerity and deformation degree in the development of barchan dunes; (v) asymmetric bidirectional winds, asymmetric inflow and interaction between dunes account for the formation of asymmetric dunes in this area.

References:

Aguera-Vega F, Carvajal-Ramirez F, Martinez-Carricondo P, Sanchez-Hermosilla lopez J, Mesas-Carrascosa FJ, & Garcia-Ferrer A. (2018). Reconstruction of extreme topography from UAV structure from motion photogrammetry. Measurement 121: 127-138.

Alvarez CA, & Franklin EM. (2020). Shape evolution of numerically obtained subaqueous barchan dunes. Physical Review E 101(1): 012905.

Anderson RS. (1990). Eolian ripples as example of self-organization in geomorphological systems. Earth-Science Reviews 29:77-96.

Andreotti B, Claudin P, & Douady S. (2002). Selection of dune shapes and velocities. Part 1: Dynamics of sand, wind and barchans. The European Physical Journal B Condensed Matter and Complex Systems 28: 341-352.

Assis WR, & Franklin EM. (2021). Morphodynamics of barchan-barchan interactions investigated at the grain scale. Journal og Geophysical Research: Earth Surface 126, e2021JF006237.

Assis WR, Cúñez FD, & Franklin EM. (2022). Revealing the Intricate Dune-Dune Interactions of Bidisperse Barchans. Journal of Geophysical Research: Earth Surface 127(5): e2021JF006588.

Baas ACW, & Delobel LA. (2022). Desert dunes transformed by end-of-century changes in wind climate. Nature Climate Change 12:999-1006.

Baddock MC, Wiggs FSG, & Livingstone I. (2011). A field study of mean and turbulent flow characteristics upwind, over and downwind of barchan dunes. Earth Surface Processes and Landforms 36: 1435-1448.

Bagnold RA. (1941). The physics of blown sand and desert dunes. London: Chapman and Hall.

Baird T, Bristow CS, & Vermeesch P. (2019). Measuring sand dune migration rates with COSI-Corr and landsat: Opportunities and challenges. Remote Sensing 11 (20): 2423.

Balek JJ. (2017). A critical evaluation of the use of an inexpensive camera mounted on a recreational unmanned aerial vehicle as a tool for landslide research. Landslides

14: 1217-1224.

Barchyn TE, & Hugenholtz CH. (2012). Predicting vegetation-stabilized dune field morphology. Geophysical Research Letters 39: L17403

Bao F, Dong ZB, & Zhang ZC. (2015). Wind regime in the Qaidam Basin Desert. Journal of Desert Research 35(3):549-554.

Beadnell HJL. (1910). The sand-dunes of the Libyan desert. Geographical Journal 35: 379-395.

Blumberg DG. (2006). Analysis of large aeolian (wind-blown) bedforms using the Shuttle Radar Topography Mission (SRTM) digital elevation data. Remote Sensing of Environment 100: 179–189.

Bogle R, Redsteer MH, & Vogel J. (2015). Field measurement and analysis of climatic factors affecting dune mobility near Grand Falls on the Navajo Nation, southwestern. Geomorphology 228:41-51.

Bourke MC, & Goudie AS. (2009). Varieties of barchan form in the Namib Desert and on Mars. Aeolian Research 1(1-2): 45-54.

Bourke MC. (2010). Barchan dune asymmetry: observations from Mars and Earth. Icarus 205:183-197.

Bristow CS. (2019). Bounding surfaces in a barchan dune: Annual cycles of deposition? Seasonality or erosion by superimposed bedforms? Remote Sensing, 11(8): 965.

Bristow NR, Blois G, Best JL, & Christensen KT. (2018). Spatial scales of turbulent flow structures associated with interacting barchan dunes. Journal of Geophysical Research: Earth Surface 124: 1174-1200.

Brown DG, & Arbogast AF. (1999). Digital photogrammetric change analysis as applied to active coastal dunes in Michigan. Photogrammetric Engineering and Remote Sensing 65: 467–474.

Bruno L, Horvat L, & Raffaele L. (2018). Windblown sand along railway infrastructures: A review of challenges and mitigation measures. Journal of Wind Engineering and Industrial Aerodynamics 177: 340-365.

Bryant RG, & Baddock MC, (2022). Remote Sensing of Aeolian Processes. In: Shroder, J.J.F. (Ed.), Treatise on Geomorphology, vol. 7. Elsevier, Academic Press, pp.84–119.

Che XH, Luo WY, Shao M, & Wang ZY. (2021). Form-flow feedback within blowout at different develop stages in the Gonghe Basin, Qinghai Province. Advances in Earth Science 36(1):1-15.

Chen YX, Yizhaq HZ, Mason JA,Zhang XL, & Xu ZW. (2021). Dune bistability identified by remote sensing in a semi-arid dune field of northern China. Aeolian Research 53:100751.

Chen ZY, Dong ZB, & Wang QQ. (2018). Wind regime and dune field patterns in the Gonghe Basin, Qinghai, China. Journal of Desert Research 38(3): 492-499. (in Chinese with English Abstract)

Cooke R, Warren A, & Goudie A. (1993). Desert Geomorphology. London: CRC Press.

Cornish V. (1914). Waves of sand and snow and the eddies which make them. T. Fisher Unwin: London and Leipsic.

Coursin A. (1964). Observations et experiences faites en avril et mai 1956 sur les barkhans du Souehel el Abiodh (region est de Port-Etienne). Bulletin de l'I. F. A. N. 26(A): 989-1022.

Ding C, Zhang L, Liao MS, Feng GC, Dong J, Ao M, & Yu YH. (2020). Quantifying the spatio-temporal patterns of dune migration near Minqin Oasis in northwestern China with time series of Landsat-8 and Sentinel-2 observations. Remote Sensing of Environment 236: 111498.

Dong GR, Gao SY, Jin J, Li BS, & Zhou GC. (1993). Land desertification and its control in Gonghe Basin, Qinghai Province. Beijing: Science press.

Dong YX, & Huang DQ. (2014). Typical research on the movement and topographic change of coastal crescent dune. Scientia Geographica Sinica 34(007): 863-869. (in Chinese with English Abstract)

Dong YX, Hesp PA, Huang DQ, & Namikas SL. (2017). Flow dynamics and sediment transport over a reversing barchan, Changli, China. Geomorphology 278:121-127.

Dong ZB, Hu GY, Qian GQ,Lu JF, Zhang ZC, Luo WY, et al. (2017). High-Altitude aeolian research on the Tibetan Plateau. Reviews of Geophysics 55. https://doi.org/10.1002/2017RG000585.

Dong, Z., Wang, X. & Chen, G. (2000). Monitoring sand dune advance in the Taklimakan Desert. Geomorphology 35(3-4): 219-231.

Durán O, Parteli EJ, & Herrmann HJ. (2010). A continuous model for sand dunes: Review, new developments and application to barchan dunes and barchan dune fields. Earth Surface Processes and Landforms 35(13): 1591-1600.

Eastwood EN, Kocurek G, Mohrig D, & Swanson T. (2012). Methodology for reconstructing wind direction, wind speed and duration of wind events from aeolian cross-strata. Journal of Geophysical Research 117(F3): F03035

Elbelrhiti H. (2012). Initiation and early development of barchan dunes: A case study of the Moroccan Atlantic Sahara Desert. Geomorphology 138(1): 181-188.

El-Sherbiny S, & Bofah KK. (1982). Measurements of the flow field over an eolian sand dune. Arab Journal for Science and Engineering 7(3): 253-260.

Ewing RC, McDonald GD, & Hayes AG. (2015). Multi-spatial analysis of aeolian dune-field patterns. Geomorphology 240:44-53.

Fearnehough W, Fullen MA, Mitchell DJ,Trueman IC, & Zhang J. (1998). Aeolian deposition and its effect on soil and vegetation changes on stabilized desert dunes in northern China. Geomorphology 23;171-182.

Fedolovich BA. (1962). Research achievements in desert research since Oboruqiev's desert exploration. Translated by Chen ZP, Origin of desert landforms and research methods. Beijing: Science Press.

Finkel HJ. (1959). The barchans of southern Peru. The journal of Geology 67: 614-647.

Frank AJ, & Kocurek G. (1966). Airflow up the stoss slope of sand dunes: limitations of current understanding. Geomorphology 17: 47-54.

Fryberger SG, Hesp P, & Hastings K. (1992). Aeolian granule deposits, Namibia. Sedimentology 39:319-331.

Gao X, Narteau C, Rozier O, & Pont SCD. (2015). Phase diagrams of dune shape and

orientation depending on sand availability. Scientific Reports 5:14677.
Gay Jr SP. (1999). Observations regarding the movement of barchan sand dunes in the Nazca to Tanaca area of southern Peru. Geomorphology 27(3-4): 279-293.
Genois M, Pont SCD, Herson P, & Gregoire G. (2013). An agent-based model of dune interations produces the emergence of patterns in deserts. Geophysical Research Letters 40:3909-3914.
Gifford AW, Warner DW, & El-Baz F. (1979). Orbital observation of sand distribution in the Western Desert of Egypt. In: El-Baz F, Warner D (Eds). Apollo-Soyuz Test Project Summary Science Report, Vol. II. National aeronautics and space Administration, Washington DC, pp:219-236.
Gillette DA, & Chen WN. (2001). Particle production and aeolian transport from a “supply-limited” source area in the Chihuahuan desert, New Mexico, United States. Journal of Geophysical Research 106(6): 5267-5278.
Gu LX, Lv P, Ma F, Chen GX, Lang Z, Xu MJ, & Yang Y. (2022). Drift potential characteristics of Mu Us Sandy Land calculated with different data sources. Journal of Desert Research 42(5) :54-62. (in Chinese with English Abstract)
Gunn A, Casasanta G, Liberto LD, Falcini F, Lancaster N, & Jerolmack DJ. (2022). What sets aeolian dune height? Nature Communications 13:2401.
Guo LC, Xiong AF, Dong XX, Ding ZL, Yang P, Zhao H, et al. (2019). Linkage between C4 vegetation expansion and dune stabilization in the deserts of NE China during the late Quaternary. Quaternary International 503:10-23.
Guo JY, Dong Z, Li JR, Shan D, Liang ZQ, Tian SM, & Chen XC. (2016). Dune morphology and migration characteristics in the Ulanbuh desert. Research of Soil and Water Conservation 23(06): 40-44. (in Chinese with English Abstract)
Guo ZC, Xie YW, Guo H, Zhang XY, Zhang XH, Xi GL, et al. (2023). Is land degradation worsening in Northern China? Quantitative evidence and enlightenment from satellites. Land Degras Development 34:1662-1680.
Hamdan MA, Refaat AA, & Wahed MA. (2016). Morphologic characteristics and migration rate assessment of barchan dunes in the Southeastern Western Desert of Egypt. Geomorphology 257: 57–74.
Han QJ, Qu JJ, Dong ZB, Zu RP, Zhang KC, Wang HT, et al. (2014). The effect of air density on sand transport structures and the adobe abrasion profile: a field wind-tunnel experiment over a wide range of altitude. Boundary-Layer Meteorology 150:299-317.
Han QJ, Qu JJ, Dong ZZ, Zhang KC, & Zu RP. (2015). Air density effects on aeolian sand movement: Implications for sediment transport and sand control in regions with extreme altitudes or temperatures. Sedimentology 62:1024-1038.
Hastenrath RJ. (1967). The barchans of the Arequipa region, southern Peru. Ztschrift Fur Geomorphologie 11(3): 300-331.
Hastenrath RJ. (1987). The barchan dunes of Southern Peru revisited. Zeitschrift fur Geomorphologie Supplementary Issues 31(2): 167-178.
Havivi S, Amir D, Schvartzman I, August Y, Maman S, Rotman SR, et al. (2018). Mapping dune dynamics by InSAR coherence. Earth Surface Processes and Landforms 43: 1229-1240.

He JL, Zhang SH, Cui W, Guo JY, Mu JJ, Chen QC, et al. (2011). Monitoring and research on aeolian sand flowed into Yellow River from Ulan Buh desert in Inner Mongolia. China Water Resources 10:46-48. (in Chinese with English Abstract)

Hersen P. (2005). Flow effects on the morphology and dynamics of aeolian and subaqueous barchan dunes. Journal of Geophysical Research: Earth Surface 110: F04S07.

Hesp PA, Castilhos JAD, Silva GMD, Dillenburg S, Martinho CT, Aguiar D, et al. (2007). Regional wind fields and dunefield migration, southern Brazil. Earth Surface Processes and Landforms 32: 561-573.

Hesp PA, & Hastings K. (1998). Width, height and slope relationships and aerodynamic maintenance of barchans. Geomorphology 22(2): 193-204.

Ho TD, Valance A, Dupont P, & Moctar AOE. (2011). Scaling laws in aeolian sand transport. Physical Review Letters 106,094501.

Huang JP, Zhang GL, Zhang YT, Guan XD, Wei Y, & Guo RX. (2020). Global desertification vulnerability to climate change and human activities. Land Degrad Dev 31:1380-1391.

Hugenholtz CH, & Barchyn T.E. (2010). Spatial analysis of sand dunes with a new global topographic dataset: new approaches and opportunities. Earth Surface Processes and Landforms 35(8): 986–992.

Hugenholtz CH, Levin N, Barchyn TE, & Baddock MC. (2012). Remote sensing and spatial analysis of Aeolian sand dunes: A review and outlook. Earth-Science Reviews 111:319-334.

Hugenholtz CH. (2010). Topographic changes of a supply-limited inland parabolic sand dune during the incipient phase of stabilization. Earth Surface Processes and Landforms 35: 1674-1681.

Hunter RE, Richmond BM, & Alpha TR. (1983). Storm-controlled oblique dunes of the Oregon coast. Geological Society of America Bulletin 94:1450-1465.

Iversen JD, Pollack JB, Greeley R, & White BR. (1976). Saltation on Mars: the effect of interparticle force, surface roughness, and low-atmospheric density. Icarus 29:381-393.

Jackson DWT, Beyers JHM, Lynch K, Cooper JAG, Baas ACW, & Delgado-Fernandez I. (2011). Investigation of three-dimensional wind flow behavior over coastal dune morphology under offshore winds using computational fluid dynamics (CFD) and ultrasonic anemometry. Earth Surface Processes and Landforms 36: 1113–1124.

James MR, Chandler JH, Eltner A, Fraser C, Miller PE, Mills JP, et al. (2019). Guidelines on the use of structure-from-motion photogrammetry in geomorphic research. Earth Surface Processes and Landforms 44:2081-2084.

Jiang C, Zhang H, Zhao L, Yang Z, Wang X, Yang L, et al. (2020). Unfolding the effectiveness of ecological restoration programs in combating land degradation: Achievements, causes, and implications. Science of the Total Environment, 748, 141552.

Jimenez JA, Maia LP, Serra J, & Moraiss J. (1999). Aeolian dune migration along the Ceara coast, north-eastern Brazil. Sedimentology 46(4): 689-701.

Kamath S, Shao YP, &Parteli EJR. (2022). Scaling laws in aeolian sand transport under low sand availability. Geophysical Research Letters 49, e2022GL097767.

Kocurek G, Townsley M, Yeh E, Havholm K, & Sweet ML. (1992). Dune and dune-field development on Padre Island, Texas, with implications for interdune deposition and water-table-controlled accumulation. Journal of Sedimentary Petrology 62(4):622-635.

Kroy K, Fischer S, &Obermayer B. (2005). The shape of barchan dunes. Journal of Physics: Condensed Matter 17: S1229-S1235.

Kuriyama Y, Moghizuki N, & Nakashima TN. (2005). Influence of vegetation on aeolian sand transport rate from a backshore to a foredune at Hasaki, Japan. Sedimentology 52:1123-1132.

Lancaster N. (1982). Dunes on the Skeleton Coast, Namibia (south west Africa): Geomorphology and grain size relationships. Earth Surf. Proc. Land 7: 575–587.

Lancaster N, & Baas A. (1998). Influence of vegetation cover on sand transport by wind:field studies at Owens Lake, California. Earth Surface Processes and Landforms 23:69-82.

Lee DB, Ferdowsi B, & Jerolmack DJ. (2019). The Imprint of Vegetation on Desert Dune Dynamics. Geophysical Research Letters 46: 12041-12048.

Leprince S, Ayoub F, Klingert Y, & Avouac JP. (2007). Co-Registration of Optically Sensed Images and Correlation (COSICorr): An operational methodology for ground deformation measurements. 2007 IEEE International Geoscience and Remote Sensing Symposium, Barcelona, Spain, pp. 1943–1946.

Levin N, & Ben-Dor E. (2004). Monitoring sand dune stabilization along the coastal dunes of Ashdod-Nizanim, Israel,1945-1999. Journal of Arid Environments 58:335-355.

Li SK. (1992). A preliminary study on the formation time of Kumkury Desert. Arid Zone Research 9(2):27-32. (in Chinese with English Abstract)

Liu B, Jin HL, Sun Z, Su ZZ, & Zhang CX. (2014). Spatiotemporal evolution of sandy land in the Gonghe Basin during the Holocene Period and its possible driving mechanism. Journal of Desert Research 34(4): 982-991. (in Chinese with English Abstract)

Liu L. (2018). The formation and evolution of aeolian environment in the Gonghe Basin. Lanzhou: Lanzhou university. (in Chinese with English Abstract)

Livingstone I. (2003). A twenty-one-year record of surface change on a Namib linear dune. Earth Surface Processes and Landforms 28:1025-1031.

Long JT, & Sharp RP. (1964). Barchan-dune movement in imperial valley, California. Geological Society of America Bulletin 75(2): 149-156.

Luo WY, Shao M, Che XH, Hesp PA, Bryant RG, Yan CZ, et al. (2020). Optimization of UAVs-SfM data collection in aeolian landform morphodynamics: a case study from the Gonghe Basin, China. Earth Surface Processes and Landforms 45(13): 3293-3312.

Luo WY, Wang ZY, Shao M, Lu JF, Qian GQ, Dong ZB, et al. (2019). Historical evolution and controls on mega-blowouts in northeastern Qinghai-Tibetan Plateau, China. Geomorphology 329: 17-31.

Lv P, Dong ZB, Narteau C, & Rozier O. (2016). Morphodynamic mechanisms for the formation of asymmetric barchans: improvement of the Bagnold and Tsoar models. Environ Earth Sci 75: 259.

Lv P, Dong ZB, & Rozier O. (2018). The combined effect of sediment availability and wind regime on the morphology of aeolian sand dunes. Journal of Geophysical Research: Earth Surface 123(11): 2878-2886.

Merwe BVD, Pillay N, & Coetzee S. (2022). An application of CNN to classify barchan dunes into asymmetry classes. Aeolian Research 56: 100801.

Mckee ED. (1979). A study of global sand seas. U.S. Geological Survey Professional Paper.

Muhs DR, & Holiday VT. (1995). Evidence of active dune sand on the Great Plains in the 19th century from accounts of early explorers. Quaternary Research 43(2):198-208.

Narteau C, Zhang D, Rozier O, & Claudin P. (2009). Setting the length and time scales of a cellular automaton dune model from the analysis of superimposed bed forms. Journal of Geophysical Research 114: F03006.

Ojeda J, Vellejo I, & Malvarez GC. (2005). Morphometric evolution of the active dunes system of the Doñana National Park, Southern Spain (1977–1999). Journal of Coastal Research SI 49: 40–45.

Parteli EJR, Duran O, Bourke MC, Tsoar H, Poschel T, & Herrmann H. (2014). Origins of barchan dune asymmetry: Insights from numerical simulations. Aeolian Research 12:121-133.

Parteli EJR, Duran O, Tsoar H, Schwammle V, & Herrmann HJ. (2009) Dune formation under bimodal winds. Proceeding of the National Academy of Sciences of the United States of America 106(52):22085-22089.

Pang YJ, Wu B, Li YH, & Xie SB. (2020). Morphological characteristics and dynamic changes of seif dunes in the eastern margin of the Kumtagh Desert, China. J Arid Land 12(5):887-902.

Pedersen A, Kocurek G, Mohrig D, & Smith V. (2015). Dune deformation in a multi-directional wind regime: White Sands Dune Field, New Mexico. Earth Surface Processes and Landforms 40(7): 925-941.

Qian GQ, Dong ZB, Luo, WY, & Wang, HY. (2009). Variations of horizontal and vertical velocities over two-dimensional transverse dunes: a wind tunnel simulation of the effect of windward slope. Journal of Arid Environments 73(12): 1109-1116.

Qian GQ, Yang ZL, Tian M, Dong ZB, Liang AM, & Xing XG. (2021). From dome dune to barchan dune: Airflow structure changes measured with particle image velocimetry in a wind tunnel. Geomorphology 382:107681.

Reitz MD, Jerolmack DJ, Ewing RC, & Martin RL. (2010). Barchan-parabolic dune pattern transition from vegetation stability threshold. Geophysical Research Letters 37: L19402.

Rim SCR. (1958). Simulations by dynamical model, of sand tract morphology occurring in Israel. Bull.Res.Counc. Israel 7-G 123-137.

Robson DT, & Baas ACW. (2023). A simple agent-based model that reproduces all types of barchan interactions. Geophysical Research Letters 50, e2023GL105182.

Ryan JA, & Henry RM. (1979). Mars atmospheric phenomena during major dust storms, as measured at the surface. Journal of Geophysical Research Solis Earth 84:2821-2829.

Sakamoto-Arnold CM. (1988). Eolian features produces by the December 1977 windstorm Southern San Joaquin Valley, California. Journal of Geology 89:129-137.

Sam L, Gahlot N, & Prusty BG. (2015). Estimation of dune celerity and sand flux in part of West Rajasthan, Gadra area of the Thar Desert suing temporal remote sensing data. Arab J Geosci 8:295-306.

Sauermann G, Rognon P, Poliakov A, & Herrmann HJ. (2000). The shape of the barchan dunes of southern Morocco. Geomorphology 36(1-2): 47-62.

Scheidt SP, & Lancaster N. (2013). The application of COSI-Corr to determine dune system dynamics in the southern Namib Desert using ASTER data. Earth Surface Processes and Landforms 38:1004-1019.

Scheltinga RCT, Coco G, Kleinhans MG, & Friedrich H. (2020). Observations of dune interactions from DEMs using through-water Structure from Motion. Geomorphology 359,107126.

Scheltinga RCT, Coco G, Kleinhans MG, & Friedrich H. (2022). Sediment transport on a sand bed with dunes: deformation and translation fluxes. Journal of Geophysical Research: Earth Surface 127, e2021JF006292.

Selby MJ, Rains RB, & Palmer RWP. (1974). Eolian deposits of the ice-free Victoria Valley, southern Victoria Land, Antarctica. New Zealand Journal of Geology and Geophysics 17(3):543-562.

Sha ZJ, Ma HZ, Li LQ, Zhou DJ, Cao GC, Ou LY, et al. (2005). Landuse and landcover changing course in Longyangxia Reservoir region of Gonghe Basin from 1987 to 1999. Journal of Desert Research 25(1):20-26. (in Chinese with English Abstract)

Shao M. (2021). Dune migration and deformation under "supply-limited" source area, a case study from the ErTala area in Gonghe Basin. Lanzhou: Northwest Institute of Eco-Environment and Resources, Chinese Academy of Sciences. (in Chinese with English Abstract)

Shao M, Luo WY, Che XH, Wang F, Lu JF, & Zou SB. (2021). Aeolian sand transport and its potential amount into Longyangxia Reservoir in 1987-2019 based on COSI-Corr. Journal of Desert Research 41(6):249-261. (in Chinese with English Abstract)

Slattery MC. (1990). Barchan migration on the Kuiseb river delta, Namibia. South African Geographical Journal 72(1): 5-10.

Smith AB, Jackson DWT, & Cooper JAG. (2017). Three-dimensional airflow and sediment transport patterns over barchan dunes. Geomorphology 278:28-42.

Smith HTU. (1966). Wind-formed pebble ripples in Antarctica. Geological Society of America special paper 87:160.

Sweet ML, & Kocurek G. (1990). An empirical model of aeolian dune lee-face airflow. Geomorphology 37(6): 1023-1038.

Tsoar H, & Parteli EJ. (2016). Bidirectional winds, barchan dune asymmetry and formation of seif dunes from barchans: a discussion. Environ. Earth Sci. 75 (18):

1–10.

Tsoar H. (1983). Dynamic processes acting on a longitudinal(seif) sand dune. Sedimentology 30:567-578.

Tsoar H. (1984). The formation of seif dunes from barchans-a discussion. Zeit. Fur Geomorphology 28:99-103.

Tsoar H. (1985). Profile analysis of sand dunes and their steady state signification. Geografiska Annaler 67 (1-2): 47-59.

Vandijk PM, Arens SM, & Boxel JHV. (1999). Aeolian processes across transverse dunes. II: Modelling the sediment transport and profile development. Earth Surface Processes and Landforms 24: 319-333.

Vermeesch P, & Drake, N. (2008). Remotely sensed dune celerity and sand flux measurements of the world's fastest barchans (Bodele, Chad). Geophysical Research Letters 35(24): L24404.

Walker IJ, & Nickling WG. (2002). Dynamics of secondary airflow and sediment transport over and in the lee of transverse dunes. Prog. Phys. Geogr. 26 (1), 47–75.

Walmsley JL, & Howard AD. (1985). Application of a boundary-layer model to flow over an aeolian dune. Journal of Geophysical Research 90(D6): 10631-10640.

Wiggs GFS, Livingstone I, & Warren A. (1996). The role of streamline curvature in sand dune dynamics: evidence from field and wind tuunel measurements. Geomorphology 17(1-3):29-46.

Wiggs GFS, Livingstone I, Thomas ASG, & Bullard JE. (1994). Effect of vegetation removal on airflow patterns and dune dynamics in the southwest Kalahari Desert. Land Degradation & Rehabilitation 5:13-24.

Wiggs GFS, Thomas ASG, & Bullard JE. (1995). Dune mobility and vegetation cover in the southwest Kalahari Desert. Earth Surface Processes and Landforms 20:515-529.

Wippermann FK, & Gross G. (1986). The wind-induced shaping and migration of an isolated dune: a numerical experiment. Boundary Layer Meteorol 36(4): 319-334.

Wu X, Zou X, Zheng ZC.& Zhang C. (2011). Field measurement and scale-down wind-tunnel model measurement of airflow field over a barchan dune. Journal of Arid Environments 75:438-445.

Wu Z. (2003). Aeolian geomorphology and sand control engineering. Beijing: Science Press, Bejing.

Xu DY, & Zhang XY. (2021). Multi-scenario simulation of desertification in North China. Land Degrad Dev 32:1060-1074.

Xu GJ, Dong ZB, & Wang ZY. (2017). Coexistence of crescent dunes and linear dunes in the Qaidam Basin of China. Journal of Desert Research 37(3):407-143. (in Chinese with English Abstract)

Xu SY, Xu DF, & Shi SR. (1982). Aeolian sand deposits in the Gonghe Basin, Qinghai Province. Journal of Desert Research 2(3): 1-8. (in Chinese with English Abstract)

Xu ZW, Mason JA, & Lu HY. (2015). Vegetated dune morphodynamics during recent stabilization of the MuUS dune field, north-central China. Geomorphology 228:486-503.

Yang JH, Dong ZB, Liu ZY, Shi WK, Chen GX, Shao TJ, et al.. (2019). Migration of barchan dunes in the western Quruq Desert, northwestern China. Earth Surface Processes and Landforms 44:2016-2029.

Yang XP, Scuderi L, Liu T, Paillou P, Li HW, Dong JF, et al. (2011). Formation of the highest sand dunes on Earth. Geomorphology 135: 108-116.

Yang ZH, Dong ZB, Liu ZY, Shi WK, Shao TJ, & Zeng HM. (2019). Migration of barchan dunes in the western Quruq Desert, northwestern China. Earth Surface Processes and Landforms 44: 2016-2029.

Yang ZL, Qian GQ, Dong ZB, Tian M, & Lu JF. (2021). Migration of barchan dunes and factors that influence migration in the Sanlongsha dune field of the northern Kumtagh Sand Sea, China. Geomorphology 378:107615.

Yang ZL. (2019). Aeolian sediment transport and dynamic evolution of barchan dunes in the Sanlongsha Dune-field. (Doctoral dissertation). Lanzhou： Northwest Institute of Eco-Environment and Resources, Chinese Academy of Sciences. (in Chinese with English Abstract)

Zhang P, Sherman DJ, Pelletier JD, Ellis JT, Farrell EJ, & Li B. (2022). Quantification and classification of grainflow morphology on natural dunes. Earth Surface Processes and Landforms 47:1808-1819.

Zhang KC, Zu RP, Qu JJ, Liao KT, & Ling YQ. (2008). Relationship between sand drift potential and maximum possible sand transport in southeast of Tengger Desert. Journal of Desert Research 28(4):605-610. (in Chinese with English Abstract)

Zhang ZC, Dong ZB, Hu GY, & Parteli EJR. (2018). Migration and morphology of asymmetric barchans in the Central Hexi Corridor of Northwest China. Geosciences 8(6): 204.

Zheng Z, Du S, Taubenböck H, & Zhang X. (2022). Remote sensing techniques in the investigation of aeolian sand dunes: A review of recent advances. Remote Sensing of Environment 271: 112913.

Zhu ZD, Chen ZP, Wu Z, Li JZ, Li BY, Wu GC, et al. (1981). Study on aeolian geomorphology of Taklimakan. Beijing: Science Press.

Zhu ZD, Guo HW, & Wu GC. (1964). Dune movement near oasis in southwestern Taklimakan Desert. Acta Geographica Sinica 30(01): 37-52. (in Chinese with English Abstract)